Dating kaolinite from the Neogene Içá Formation and overlying laterites, central Amazonia, Brazil: Constraints for a stratigraphic correlation

Thierry Allard, Luciana Pereira, Maximilien Mathian, E. Balan, Guilherme Taitson Bueno, Christophe Falguères, Nadia Regina Do Nascimento

Dating kaolinite from the Neogene Içá Formation and overlying laterites, central Amazonia, Brazil: constraints for a stratigraphic correlation.

Allard T. *[(1)], Pereira L. [(2)], Mathian M. [(1)], Balan E.[(1)], Taitson Bueno G. [(3)], Falguères C.[(4)], do Nascimento N.R. [(4),]

[(1)] IMPMC, UMR CNRS 7590, Sorbonne Université, Paris, France

[(2)] CPRM, Serviço Geológico do Brasil, Brazil

[(3)] UFG, Universidade Federal de Goiás, Brazil

[(4)] IPH, UMR7194, 1 rue René Panhard, Paris, France,

[(5)] UNESP, Universidade Estadual Paulista, Rio Claro, Brazil

*corresponding author

email: thierry.allard@upmc.fr

tel.: 33 1 44 27 98 20

fax: 33 1 44 27 37 85

Abstract

The Neogene Içá Formation is a major sedimentary deposit in central Amazonia (Brazil) that is critical to the understanding and modeling of the evolution of the Amazon Basin. However, its chronostratigraphy is poorly defined, mostly because it is not fossiliferous and it does not contain volcanic ash levels. This study is the first attempt at the absolute dating of the sediments and overlying soils of the Içá Formation by electron paramagnetic resonance (EPR) of radiation-induced defects in kaolinite (RIDs). Four profiles of unconsolidated sediments overlaid by lateritic soils from the Barcelos region (Amazonia, Brazil) were studied. The concentration of RIDs was assessed from EPR spectra through a simplified procedure on a selected set of samples, excluding those showing too strong of interference from the signal of trace vanadyl complexes. It is shown that in such sedimentary material, both the microscopic distribution of thorium (together with uranium) and the origin of kaolinite, either detrital or authigenic, are critical for kaolinite dating. Considering an argued authigenic origin and two scenarios of Th distribution, it appears that most of the present chronologic data support the stratigraphic correlation with the Madre de Dios sedimentary Formation in Peru previously proposed in the literature for the Içá Formation (9.5 – 2.5 Ma). This study also shows a rejuvenation process of kaolinite both in the uppermost soil and at depth of the profiles. This rejuvenation occurred during paleoclimatic periods already revealed in other weathering covers from the Amazon Basin and possibly resulted from downward weathering in the topsoil and water table or lateral weathering at depth

Keywords: geochronology; electron paramagnetic resonance; dosimetry; artificial irradiation; radiation-induced defects; sediments

47

48 1. Introduction

49 Explicative and predictive models of the evolution of continental surfaces require the
50 dating of sediments and soils in relation to the influence of geologic events such as
51 orogeneses and thus tectonic plate drifts, local paleoclimates and paleogeography. Among the
52 greatest basins in the world is the Amazon Basin, which represents 40% of the South
53 American subcontinent. It is deeply seated on Paleozoic craton and sediment deposits (Hoorn
54 and Wesselingh, 2010). In the Brazilian section of the basin, the weathering covers consist
55 mainly of laterites that developed on various parent rocks and represent 80% of the basin area,
56 according to th Projeto Radam documents (Projeto Radam, 1972-1978; Fritsch et al. 2011 and
57 references therein). The long-term history of the Amazon Basin is described by increasingly
58 detailed geologic and palaeogeographic studies (see Hoorn and Wesselingh, 2010). The
59 present concerns include, e.g., explaining the great biological diversity of Amazonia (Hoorn
60 et al., 2010) and determining the ages and conditions of genesis of natural resources such as
61 kaolins of sedimentary or pedologic origin (da Costa et al., 2009, Sousa et al., 2007, Montes
62 et al., 2007; Lucas et al., 2012). The Neogene represents a particularly noticeable period in the
63 history of the Amazon Basin because it coincides with the development of the modern
64 eastward Amazon River system (Horbe et al., 2013; Rossetti et al. 2015).

65 In this work, we focus on the dating of unconsolidated sediments occurring at the
66 regional scale and assigned, from our detailed observations in the field and from remote
67 sensing maps, to the Neogene Içá Formation in Brazil, which crops out widely in the central
68 Amazon Basin (Figure 1). Its still disputed area may reach 1.000.000 km^2 (Fritsch et al.,
69 2011; CPRM, 2010). It occurs at approximately 100-140 m a.s.l. and lies unconformably on
70 the Solimões Formation. The chronostratigraphy of the Içá Formation in Brazil is poorly
71 known owing to the lack of fossils or datable material such as volcanic ash within it.

However, it is assumed to correlate with another formation in Perù, the Madre de Dios Formation, which developed after the Pan-Amazonian Ucayali Peneplain at the beginning of the Quechua II orogenic event (Campbell et al., 2006). The Madre de Dios Formation was deposited between 9.5 Ma and 2.5 Ma, as assessed from the dating of local ash levels in circumscribing levels (Campbell et al., 2006).

Thus far, it has not been possible to perform absolute dating of the Içá Formation itself with K-Ar in volcanic ash or in K-bearing manganese oxides, but one of its main components, i.e., kaolinite, may be considered a potential geochronometer. Kaolinite contains radiation-induced defects (RIDs) that accumulate with time as a result of ambient radioactivity (Clozel et al., 1994). Consequently, RIDs can be used in various geological applications (Muller and Calas, 1989; Muller et al., 1992; Allard et al., 2012), especially as geochronometers in tropical weathering covers such as laterites (Balan et al., 2005, Allard et al., 2018; Mathian et al., 2019). The time range covered by this approach is consistent with geological periods and is appropriate for dating kaolinite-containing tropical sediments and soils. In a previous study, one sample of iron duricrust developed on Içá sediments was dated by electron paramagnetic resonance spectroscopy of trapped kaolinite particles, yielding an age of 1.7-4.0 Ma (Allard et al., 2018). An important difficulty in dating detrital sediment deposition arises when these sediments are preserved from diagenetic transformations. In this situation, the kaolinite may not have formed in the sediment during or just after deposition but previously in the soils (possibly laterites) that predated erosion, transport and deposition in the basin. Consequently, the methodology for detrital kaolinites potentially overestimates deposition ages, except when the residence time in uphill soils (i.e., as the source of eroded and deposited material) is negligible with respect to the age of the sediment deposition. Thus, authigenic or detrital origins of clay minerals must be documented to enforce the challenging task of dating recent sediments using kaolinite.

97 The main objectives of this study are to estimate the ages of some deposits from the
98 Içá Formation and overlying soils collected in the central Amazon Basin. Subsequently, the
99 data are compared to the time range determined for the analogous Madre de Dios Formation
100 by Campbell et al. (2006) to question the stratigraphic correlation between these formations
101 and to discuss the proposal that the Içá Formation was deposited between the major events
102 corresponding to the Ucayali peneplanation and the eastward setting of the Amazon drainage.
103
104 2. Geological background
105 As stated by Hoorn and Vonhof (2006), the Neogene history of Amazonia remains obscure,
106 mainly because of the difficulty of finding relevant outcrops and because of scarce
107 chronostratigraphic determinations. For example, the determinant period of the eastward onset
108 of the Amazon system that occurred in the late Miocene or Pliocene has been debated many
109 times (see, e.g., Figueiredo et al., 2009 and Campbell, 2010). Among major geologic units,
110 the Içá Formation covers a large part of central Amazonia, although its actual extent remains
111 controversial, extending over 300,000 (Rossetti et al., 2005), 500,000 (de Souza et al., 2013)
112 and up to 1,000,000 km^2 (CPRM, 2010) (Figure 1). The Içá Formation was first described by
113 Maia et al. (1977) as a continental sedimentary series deposited in a fluvial context and
114 located in the Amazonas state, Brazil (Reis et al., 2006). It covers the Solimoes Formation
115 corresponding partly to the large wetland Pebas paleoenvironment (10-11 Ma Miocene
116 sediments, Latrubesse et al., 2007) and is deposited above the widespread erosive Ucayali
117 unconformity that marks the Quechua II tectonic phase of the Andes (Campbell et al., 2006).
118 Sediments from the Içá Formation consist of unconsolidated sands with silty and clayey
119 lenses exhibiting various sedimentary patterns including cross-bedding and ripple marks
120 (Horbe et al., 2013). According to de Almeida et al. (2016), the Içá Formation also contains
121 large sedimentary structures that correspond to barchanoid dunes settled as deep channel

deposits. Primary detrital minerals indicate that the main sediment source areas include Mesoproterozoic regions from the Amazonian craton and adjacent NW to SW provinces together with some Andean contribution (Horbe et al., 2013).

Dating studies on the Içá Formation are scarce and provide inhomogeneous data. Sediments from the Içá Formation were first thought to be Plio–Pleistocene based on stratigraphic correlations (Maia et al., 1977) or pollen studies (Latrubesse et al., 1994; Rossetti et al, 2005). In addition, absolute dating by optically stimulated luminescence of sediments from central, southwestern and northern Amazonia yielded recent ages corresponding to tens to hundreds of thousands of years before the present, i.e., within the Pleistocene period (Rossetti et al., 2015; Passos et al. 2020), in line with the Pleistocene-Holocene ages proposed by Rossetti et al. (2005). The Içá Formation was also stratigraphically correlated to the Madre de Dios Formation in Peru (Campbell, 2006), which consists of unconsolidated fluvial sands and sediments accumulated in a mega-lake complex (deltaic and fluvial-lacustrine) in its uppermost horizons. The Madre de Dios Formation was dated using $^{40}Ar/^{39}Ar$ on volcanic ash occurring at the top and bottom of the sedimentary sequence (Campbell, 2001). The sediments started to be deposited before 9 Ma and ended after 3.1 Ma, providing time constraints for important paleofaunas from the Amazon Basin. Subsequently, it was proposed that the analogous, stratigraphically correlated Içá Formation from Brazil was deposited in this period in the time range of approximately 9.5 – 2.5 Ma (Campbell et al., 2006). The model by Campbell et al. (2006) also stated that the Amazonian Basin behaved as a single sedimentary basin during this period and that the modern Amazon system began forming at the end of the Pliocene, approximately 2.5 Ma ago.

3. Materials and methods

147 3.1. Selected profiles

148 The selected sediments belong to a regional formation that we assign to the Içá
149 Formation. In fact, because of the presence of unconsolidated sediments in the entire region
150 and their location in the landscape with respect to the plateau, their facies could not be
151 confused with terraces, floodplains or modern alluvial deposits of limited extent. These
152 observations are supported by the geological map of the region produced by the
153 CPRM(Figure 1). Four selected sedimentary profiles occur in a sequence from upstream to
154 downstream of the Demini River, north of Barcelos to the Rio Negro bank. All of them are
155 composed of interspersed levels of unconsolidated clayey and sandy sediments more or less
156 impregnated with iron oxides and overlaid by oxisols (Figure 2). The four P1, P2, P3, and P4
157 profiles were named according to the closest human inhabited localities. The first profile is P3
158 (*Acampamento*), located on the right bank of the Demini River (0°15'52.1"N, 62°46'20.0"W;
159 elevation: 45 m). The P2 profile is named *Tabocal* and outcrops 50 km downstream and south
160 of Profile 3 (0°02'52.8"S, 62°45'41.5"W, elevation: 46 m). The P1 profile (*Sumaúma)* is
161 approximately 45 km downstream of Profile 2 (0°22'00.9"S, 62°46'28.7"W. Elevation: 35 m).
162 The P4 profile (*Tucandeira*) is on the right side of the Rio Negro River (1°02'41.8"S,
163 62°49'09.5"W. Elevation: 20 m) downstream of Barcelos city and the Demini River mouth
164 (Figure 1, Figure 2).

165 The base levels of profiles suggest some similarities with the A subunit proposed by
166 Campbell (2006), owing to, e.g., the occurrence of fossil plants or coarse sand layers.
167 However, the three horizons tentatively proposed by this author are not clearly distinguished
168 in the 4 studied profiles, which are much shallower (10-17 m) than the reference profiles from
169 the Madre de Dios Formation and may be eroded, weathered, only partly outcropping or
170 exhibiting lateral differentiation of facies.

171

172 3.2. Collection and preparation of samples

173 All the samples were deferrated with citrate-dithionite-bicarbonate reagent, following
174 the procedure described in Mehra and Jackson (1960), to minimize the interference of iron
175 oxides during the EPR analysis. The fraction < 5 μm was separated by size sorting in
176 sedimentation columns to concentrate the kaolinite.

177 The kaolinite GB1 from St Austell, Great Britain (Allard et al., 1994) was used as a
178 reference for the signal of RIDs. A reference VO^{2+}-rich dickite, Dimex, originating from
179 Mexico, was also used to assign the resonances of the vanadyl complex in the spectra of Içá
180 samples.

181 3.3. Chemical analyses

182 The concentrations of U, Th and K were measured in raw samples ground below 80
183 μm by ICP-AES and ICP-MS techniques at the Service d'Analyse des Roches et des
184 Minéraux (SARM at the Centre de Recherches Pétrographiques et Géochimiques,CRPG,
185 Nancy, France). Analytical details and errors regarding the measurements are described at
186 http://www.crpg.cnrs-nancy.fr/SARM/index.html.

187

188 3.4. Irradiation

189 - He^+ irradiation: The samples were deposited on stainless steel plates and irradiated
190 with 1.5 MeV He^+ ions in the Aramis linear accelerator (Centre de Sciences Nucléaires et de
191 Sciences de la Matière (CSNSM), Orsay, France). The range of 1.5 MeV He^+ ions in kaolinite
192 is 4 μm, as calculated with the SRIM code (Ziegler et al., 2010). Thus, samples of kaolinite
193 were deposited by sedimentation on stainless steel plates with a thickness of 4 μm so that all
194 the ion beam energy was absorbed in the clay mineral structure. The irradiated samples were
195 subsequently heated for 2 hours at 250 °C to anneal the unstable defects, according to the
196 procedure of Allard and Muller (1998). Dosimetry curves were derived from irradiations in

197 the 3.10^{11} - 10^{13} ions/cm^2 fluence range corresponding to doses within the range of 70 - 2342
198 kGy, which appeared to be appropriate for most conditions in lateritic covers (Balan et al.,
199 2005; Allard et al., 2018; Mathian et al., 2019).
200 - Neutron irradiation: Thin sections of selected samples were irradiated by thermal
201 neutrons to produce induced fission tracks and subsequent U mapping at the microscopic
202 scale (see, e.g., Price and Walker, (1963) for the related methodology). This was performed
203 on the FRMII reactor, Munich, Germany, according to the procedure by Sélo (1983), by
204 putting a Kapton film on the thin section before irradiation. A cumulative flux of 6.9 x 10^{15}
205 neutrons/cm^2 was used during irradiation. The fission tracks formed in the Kapton foils were
206 revealed through reaction with a hypochlorite solution (14% NaClO and 12% NaCl) at 100 °C
207 for 9 min. Then, the tracks were counted using an optical microscope with a x 1000
208 magnification. The homogeneity of the neutron flux was verified using a standard of 50 ppm
209 uranium in glass provided by the National Institute of Standards and Technology.
210
211 3.5. Electron Paramagnetic Resonance
212 Electron paramagnetic resonance spectroscopy (EPR) is a very sensitive method that
213 allows the detection of paramagnetic species, i.e., species with unpaired electrons. This
214 concerns, e.g., several ions of transition elements (Fe^{3+}, V^{4+}, Cr^{3+}, Mn^{2+}…) together with free
215 radicals (Ikeya, 1993). EPR spectra were recorded on kaolinite powder samples in the X-band
216 (≈ 9.4 GHz) at ambient temperature with a Bruker EMXplus™ spectrometer. The acquisition
217 parameters were set as 3 or 5 Gauss (1 Gauss = 10^{-4} Tesla) for the modulation amplitude of
218 the radiation-induced defects (RID) or structural Fe^{3+} species, respectively, and 40 mW for
219 microwave power. The data were normalized for sample mass, receiver gain and a constant
220 resonant cavity filling factor. The EPR spectra were defined by their effective spectroscopic
221 factor g values derived from the resonance condition:
222 $h\nu = g\beta H_0$ (1)

where h is the Planck constant; ν is the resonance frequency; g is the Landé factor, which is a tensor with eigenvalues g_{xx}, g_{yy}, and g_{zz}; β is the Bohr magneton; and H_o is the external magnetic field. The principal values of g were checked by comparison with a GB1 kaolinite used as a standard for RIDs (Allard et al., 1994).

The concentrations of radiation-induced defects in kaolinite were estimated from a measurement of the maximum amplitude of the EPR spectra in the 3300-3700 Gauss range and expressed in arbitrary units. The error in the radiation-induced defect concentration was ± 10%, taking into account the mass, positioning in the cavity, and apparatus deviation.

3.6. Gamma spectrometry

Seven raw soil and sediment samples from the four profiles (see Table 1) were selected for measurement of activities of isotopes from the uranium and thorium decay chains to estimate the possible Rn loss or gain and the resulting correction of the dose rate (Yokoyama and Nguyen, 1980). The analysis was performed by high-resolution low background gamma-ray spectrometry using a germanium detector at low temperature. The ^{238}U content was measured by a gamma ray of ^{234}Pa (its daughter) at 63.3 keV. The ^{232}Th was measured by the peaks of ^{228}Ra (^{228}Ac at 911.1 keV) and ^{228}Th (^{208}Tl at 583.2 keV representing 35% of disintegration of ^{212}Bi). To estimate the possible Rn loss or gain and the resulting correction of the dose rate, ^{226}Ra was measured by radiation at 186.1 keV, and radon (^{222}Rn) was determined using the peaks of ^{14}Bi at 609 keV and ^{214}Pb at 352 keV (Yokoyama and Nguyen, 1980).

3.7. Paleodose determination

The artificially irradiated samples were heated at 250 °C for 2 hours to anneal the less stable defects according to the procedure of Allard et al. (1994) and Balan et al. (2005). Then,

248 depending on the sample, the experimental dosimetry data (i.e., concentration of defects
249 versus dose) were fitted using either a single exponential function (e.g., Allard et al., 1994) or
250 the combination of an exponential and linear function (Duval, 2012):

251 $$[C] = [Cs](1-\exp(-\lambda (D+P))) \quad (1)$$

252 $$[C] = [Cs](1-\exp(-\lambda(D+P))) + LF\ (D+P) \quad (2)$$

253 where [C] is the present concentration of RIDs, [Cs] is their saturation value, λ is an
254 efficiency exponential factor, P is the paleodose, D is the artificial dose and LF is a linear
255 factor.

256

257 3.8. Dating

258 In the absence of significant thermal resetting, the paleodose is then linearly related to
259 the dose rate, and the kaolinite age is obtained as:

260 $$\text{Age} = \text{Paleodose/Dose-rate} \quad (3)$$

261 The dose rate can be calculated using the U, Th and K contents measured by ICP-AES
262 and ICP-MS techniques and tabulated elementary values provided by Aitken (1985).

263

264 4. Results and discussion

265 4.1. U/Th geochemistry

266 The radiation-induced defects are produced by the radiation arising mainly from U and Th
267 decay chains and, to a lesser extent, from the ^{40}K isotope. Consequently, geochemical data on
268 these elements are required to constrain the calculation of the dose rate experienced by the
269 clay minerals. The weight concentrations are as follows. For uranium, the concentration
270 varies from approximately 0.5 to 4.7 ppm. The concentration of thorium ranges from 2 to 15.9
271 ppm. That of potassium is between 0.01 and 1.37% of K. These concentrations correspond to
272 standard values for laterites or sediments derived from laterites (see, e.g., Chabaux et al.,

2003; Sousa et al., 2007; da Costa et al., 2014; Balan et al., 2005). The concentrations of U and Th show a linear dependence (Figure 3). This suggests that, except for a few data indicated in Figure 3 that are distant from the linear trend, uranium and thorium are associated with the same clay fraction and are possibly hosted by the same phases. As thorium is classically considered a geochemically invariant element, it is inferred that no preferential migration of U (i.e., loss or accumulation) occurred in the profile. The observed correlation thus implies that the most labile fraction of uranium was leached away soon after sediment deposition or in the material that predated the deposition.

4.2. Mineralogic and petrographic observations using optical and scanning electron microscopy

The mineralogy of the <5 μm samples is revealed by XRD powder patterns (Figure SI 1). It is clearly seen for sediments and soils that kaolinite is by far the dominant secondary mineral. Illite is negligible except in the P4 profile and the P1-620 sample, where it is minor. The potential consequences of such a composition with minor illite are discussed in the EPR results section. In addition, the samples from the P4 profile as well as the P2-240 soil sample contain significant amounts of quartz. Moreover, the long-range crystalline order of the kaolinites can be assessed on the XRD patterns through, e.g., the Hinckley ordering index (Hinckey, 1963). Thus, the (1-10) and (11-1) peaks at approximately 24 degrees (2 theta) are almost absent (see Figures SI 1A and SI 1B), which indicates a very low Hinckley index and thus a strong disorder. This estimate is independent from the assessment of short-range disorder through EPR (see below).

Thin sections are typical of unconsolidated sands with dominant quartz minerals in a clayey matrix (Figure 4 A,B). In addition, localized iron oxides are observed with surrounding diffuse haloes of irregular shape (Figure 4 A,B). This latter facies indicates postdeposition

298 weathering of iron oxides. The clay matrix does not exhibit well-ordered kaolinite crystals at
299 the scale of optical microscopy. This is in contrast to what is observed, e.g., in transformed
300 sediments from the older Alter do Chao Formation (Balan et al., 2005; Lucas et al., 1996) or
301 deposits at the base of weathering profiles from the eastern Amazon (Sousa et al., 2007; da
302 Costa et al., 2009). The presence of well-structured kaolinite booklets several tens of microns
303 in size would be a clear indication of authigenic origin because such particles would certainly
304 not have resisted erosion and transport processes before deposition.

305 SEM observations show ubiquitous small (<1 μm) kaolinite phases (often present with
306 traces of potassium), as shown for P1-760 and P4-1000 in Figure 4 (D-F). Kaolinite is a
307 phyllosilicate with a microscopic structure arranged as platelets, particularly visible in the
308 case of well-ordered kaolinites that often display a booklet-like arrangement. Scarce booklets
309 of several microns are also observed that are not tightly joined (Figure 4, E) or have small
310 thicknesses (Figure 4, F). This suggests some degree of structural damage tentatively assigned
311 to limited transport of particles. However, nothing conclusive can be inferred about the
312 detrital or authigenic origin of the associated, dominant, fine particles of kaolinite.

313 Mapping of uranium derived from induced fission track experiments is shown for one
314 representative sample P4-1000 in Figure 4 C. There is a clear contribution from uranium-
315 bearing or uranium-trapping minerals that could be, for instance, zircon grains ("urchin"-like
316 track clusters with radial orientation (central part of Figure 4 C) or iron oxides (composite
317 group of tracks with multiple orientations (not shown)). The rest of the uranium is associated
318 with the clayey matrix (isolated tracks, Figure 4 C). Track counting in the selected areas
319 allows the measurement of the proportion of these two fractions of uranium, either clustered
320 or dispersed, as reported in Table 1 for the matrix component. This proportion is used for the
321 correction of the dose rate (see 4.4.2 section).
322

4.3. EPR spectra of soil and sediment samples

The full-range EPR spectra of the sediment and soil samples (Figure SI 2) exhibit the classical signals observed in natural kaolinite samples (see, e.g., Muller and Calas, 1993). The so-called Fe(I) and Fe(II) signals at low magnetic fields (g≈4.3) are typical of structural Fe^{3+}. They arise from two different structural site geometries related to variations in kaolinite stacking order. Accordingly, the relative amplitude of the Fe(I) signal to that of the Fe(II) signal (Figure 5) can be used as an index of structural disorder (see, e.g., Balan et al., 1999, 2007). Most samples show quite similar spectra for structural Fe^{3+} within each profile, indicating a medium degree of local crystalline disorder. Sample P3-340 and all those from the P4 profile are more disordered, as attested by a stronger contribution of the Fe(I) resonance (Figure 5). The P4 profile belongs to a watershed located on the right bank of the Rio Negro and, according to its mineralogy (constant presence of illite), is expected to correspond to different material sources deposited in a sub-basin. Moreover, it cannot be excluded that illite, observed in this profile, also partly interferes in the samples from the P4 profiles, as this clay mineral exhibits a dominant resonance located at the position of Fe(I) (Morichon et al., 2008). Proceeding in further detail, the fine observation of the shape of the structural Fe^{3+} spectrum, i.e., the relative contributions of the Fe(I) and Fe(II) signals, allows the determination of four groups of sedimentary kaolinite populations according to their degree of disorder (Table 1), which is critical information for dosimetry (see Allard and Muller, 1998). In fact, a relationship was shown between the dosimetry parameters, i.e., the behavior under irradiation, and the degree of local structural disorder. Consequently, it is assumed that kaolinite samples with the same degree of local disorder (as determined using the structural, paramagnetic Fe^{3+} as a local probe) have similar dosimetry curves or efficiencies, albeit with different paleodoses, as this last parameter depends on age and radioactivity.

In addition, the strong signal responsible for the baseline is assigned to superparamagnetic iron oxides *lato sensu*, i.e., irrespective of their actual structure or composition (Muller and Calas, 1993).

In the g=2 region, at and from either side of the 3530 Gauss magnetic field value, several narrow signals are observed. An enlarged view of this region is shown in Figure 6, which exhibits the typical hyperfine structure of the vanadyl complex associated with kaolinite, with outermost parallel components and central perpendicular components (Muller and Calas, 1993), which can be identified with the reference VO^{2+}-rich dickite (Dimex). The corresponding signal is present in most samples. Only two samples, P1-350 and P4-1000, have a negligible or no VO^{2+} signal (Figure 6). In these cases, the observed doublet with principal components at g_{par} = 2.049 and g_{perp} = 2.002 is characteristic of RIDs in kaolinite, as seen by comparison to the GB1 reference kaolinite. For vanadyl-containing kaolinite, the central VO^{2+} signal overlaps the spectrum of RIDs. The amplitude of the g_{perp} = 2.002 signal of RIDs was thus estimated by subtraction of the overlapping vanadyl signal. For this purpose, the contribution of vanadyl was evaluated using the Dimex reference and the isolated $g \approx 1.881$ resonance, which is assigned to VO^{2+} only (Figure 6, Figure SI 3). As seen in Table 1, the proportion of RID signals in the g = 2 resonance for the selected samples was significant (> 25%) and often major. Using this procedure, 6 samples of soils and 10 samples of sediments could be selected for the present study. Their RID content corrected from the vanadyl contribution is reported in Table 1. They include two samples with 100% RID signals (P1-350 and P4-1000). The presence of minor illite may potentially interfere with the kaolinite RID signal in the P4 profile, as this clay mineral can contain RIDs very similar to the kaolinite ones (Allard et al., 2012) that cannot be isolated in the X-band. Consequently, in this case, we assumed that the potential RIDs in illite behaved similarly to those in kaolinite in terms of dosimetry, so their contribution remained minor. Based on their location in the

profiles, their degree of kaolinite crystalline disorder, their significant RID concentrations and their origin in both soils and sediments, seven samples were chosen for artificial irradiation.

4.4 Dating

4.4.1 Dosimetry curves

The concentrations of RIDs as well as the dosimetry parameters derived from data fitting are reported in Tables SI 4 a,b. The concentrations of defects are plotted as a function of irradiation dose in Figure 7. The natural concentration of RIDs, after correction of the VO^{2+} interference, corresponds to the first point of the dosimetry curve. It varies within 0.8 – 5.9 (arbitrary units), i.e., over one order of magnitude. Two types of growth curves are observed, corresponding to exponential (Equation 1) or exponential plus linear (Equation 2) functions. Although classical (see, e.g., Mathian et al., 2019), the actual origin of these two different behaviors under irradiation has not yet been elucidated. For the samples that were not artificially irradiated, the reference dosimetry parameters of the same group, identified from structural order parameters, were used to calculate the paleodoses. Within the same structural group, references from soils were used for soil samples, and data for sediments were used for sediments. In the case of sediment group I, two sets of extrapolation parameters were available, corresponding to P1-350 and P1-760. The resulting paleodoses may vary over a factor of 2.6, as seen for P2-660, P2-900, and P3-210 (Table 1). Based on these data, the uncertainty of the paleodose resulting from extrapolation is at least 50% around the average value. The resulting paleodoses vary within 10.92 to 133.92 kGy, i.e., over one order of magnitude (Table 1). Within each profile, the lowest paleodoses are observed for the soil samples. The average error for the paleodose in the cases for which irradiation could be performed is considered to be 20-30% according to the estimates of Allard et al. (2018) and Mathian et al. (2019).

398

399 4.4.2. Assessment of dose rates

400 To determine the age of kaolinite samples, it is necessary to calculate the dose rate that
401 prevails in each sample. The raw dose rate is calculated from the tabulated elementary dose
402 rates for U, Th and K and the concentrations of these elements (see, e.g., Aitken, 1985) prior
403 to several corrections detailed below.

404 The first correction addresses the opening of the geochemical system that may affect
405 the dose rate. As the samples correspond to unconsolidated sediments with connected
406 porosity, a degree of system opening was expected, which may dominantly arise from Rn loss
407 or gain, as this element is an inert gas with little interaction with solids. Because radon loss
408 disrupts the decay chains of natural U and Th, the dose rate for open systems can be
409 significantly lower than that of closed systems. In contrast, if Rn accumulates, the dose rate
410 may be higher than that expected from the measured U concentration in a closed system at
411 secular equilibrium. The gain or loss of Rn in reference samples was estimated from the
412 gamma spectrometry data, providing the values reported in Table 1. In the sample series, the
413 extreme values are 35% (increasing dose rate) for Rn gain and – 9% for Rn loss (decreasing
414 dose rate). Interestingly, these significant Rn gains and losses are observed in the soil and
415 sediment samples, respectively.

416 The second correction arises from the geometry of the system according to two factors
417 derived from the presence of minerals such as quartz that do not host radioelements. On the
418 one hand, quartz crystals are diluting agents for the effective concentration of radioelements,
419 so the dose rate must be increased and normalized to the clayey matrix (kaolinite) content. In
420 fact, quartz crystals are considered to contain no or negligible U, Th-bearing inclusions,
421 according to observations with optical or scanning electron microscopy. The concentration of
422 radioelements in the clay fraction is higher than that in the bulk quartz-containing sample. On

423 the other hand, a part of the dose is deposited in quartz and does not affect the clay. To
424 account for the factors that modify the dose rate, a simple model (SI 5) was used to assess the
425 correction as a function of the range of radiation, size of quartz grains and concentration of
426 clayey matrix (kaolinite). It concerns only alpha particles, the average range of which (20 μm
427 in silicates) is much smaller than the diameter of quartz grains. The average size of the quartz
428 grains was assessed on thin sections and, when thin sections were not available, by
429 considering the same values for close samples in the profiles (SI 6). Correction concerning
430 alpha particles in U and Th decay chains was solely considered because the dose rate linked to
431 this radiation totals 90% of the total dose rate in an infinite closed system (Aitken, 1985). The
432 concentration of the clay phase was estimated from the Al_2O_3 concentration of the raw
433 samples (see Table 1 and Figure SI 7 for sediments) by assuming that kaolinite was the
434 dominant Al-bearing phase, which was verified for most samples by XRD (Figure SI 1). In
435 fact, all samples from the P1, P2, P3 profiles contain only traces of illite. Nevertheless, the
436 kaolinite content of some samples may be overestimated: P3-465 actually contains significant
437 gibbsite content in addition to kaolinite, and the P4 samples also contain minor illite.

438 The third correction to the dose rate arises from the spatial distribution of uranium.
439 This element may occur either concentrated in host minerals or dispersed in the matrix. U-
440 bearing phases are revealed by induced fission track mapping as concentrations with radial
441 distributions ("urchin"-like) that induce a specific balance of alpha radiation dose (Figure
442 4C). The alpha particles have a mean energy of 5 MeV in the uranium decay chain, which
443 corresponds to a 20 μm range in silicates as calculated from the SRIM code of radiation –
444 matter interaction (Ziegler et al., 2010). In contrast, the ranges of beta and gamma radiation
445 are millimetric and deca-centimetric, respectively. Consequently, the alpha particles only
446 concern a thin rim around the U-bearing minerals and do not interact with the bulk clay
447 sample. Thus, for U-bearing minerals, the contribution of alpha particles is not considered in

448 the dose rate calculation corresponding to the bulk samples analyzed by EPR, leading to a
449 lower effective dose-rate value. The proportion of uranium concentrated in minerals or
450 dispersed in the matrix, as determined from fission track analysis (FT), was used to correct
451 the dose rate experienced by the kaolinite. Seven samples were selected for the FT analysis.
452 The resulting values of the U proportion in the matrix are 26.1 – 57.9% (Table 1). The values
453 for the samples not analyzed by fission tracks were determined in this range of values by
454 considering the closest soil samples between them on one side and the sediments on the other
455 side in the same profile. No model value of the proportion of U in the matrix was taken from
456 another profile or from a soil to a sediment (Table 1). In the case of P1-530 and P1-620, two
457 model values were available (from P1-350 and P1-760); thus, their average value was
458 considered. P1-530, P2-530 and P2-900, which were distant from the U/Th chemical trend,
459 have the highest U% in the matrix. In contrast, some samples with high U% in the matrix are
460 not anomalous in the U/Th trend. The average water content is estimated to be 20% according
461 to the study on laterite water content by Bruno et al. (2006), which implies a 20% decrease in
462 the dose rate (Hennig and Grun, 1983). In addition to uranium, the spatial distribution of
463 thorium is critical for the calculation of dose rate, as its concentration is significantly higher
464 (Table 1). However, these data cannot be easily obtained with the current equipment, owing
465 to the trace content of thorium (approximately 4-20 ppm in our study). Consequently, two
466 scenarios were considered herein: a homogeneous distribution in the matrix (named Th_{HOMO})
467 or a spatial distribution similar to that determined for uranium by induced FT (referred to as
468 Th_{vsU}). The first scenario is supported by the well-known low solubility of thorium, which
469 explains why this element is often used as a geochemical invariant in the weathering mass
470 budget of laterites (see, e.g., Braun et al., 1993; Balan et al., 2001), whereas the second
471 scenario is supported by the common association of U and Th to similar accessory minerals
472 such as zircon or monazite.

The resulting dose rates, i.e., after the different abovementioned corrections, are reported in Table 1. The error in the dose rate is estimated to be 10%, according to the analytical errors in the U, Th, and K concentrations.

4.4.3 Ages of soils and sediments

The calculated ages of the soils and sediments from the Içá Formation are reported in Table 1. They vary from 0.6 to 19.6 Ma, i.e., over one order of magnitude. The average age for the soils is 2.98 Ma (0.9 – 5.0 range) for Th_{vsU} and 2.07 Ma (0.6-3.5 range) for Th_{HOMO}. For the sediments, it is 9.37 Ma (4.2 – 19.6 Ma range) for Th_{vsU} and 6.56 Ma (2.3-15.1 Ma range) for Th_{HOMO}. As expected, the ages from the Th_{vsU} scenario are significantly older than those from the Th_{HOMO} scenario. In both scenarios, it is verified that the soils are younger than the sediments, which is expected given that the former overlie the latter. In addition, there is no simple relation as a function of depth except for an increasing trend in the sediment followed by a decreasing trend as the supergene weathering begins to affect the sediment.

In this study, we consider an authigenic origin of kaolinite. The materials from our sequence do not correspond, in terms of crystal chemistry of structural iron, to detrital eroded soils such as those described by Balan et al. (2005). Other arguments support authigenic origin. In particular, the P1, P2 and P3 profiles exhibit younger material both in the topsoil and at depth. This nonmonotonous evolution as a function of depth suggests rejuvenation processes of kaolinite both at the surface (soil formation) and at the bottom of profiles. The weathering at depth may have occurred as a result of another front, in line with Nahon (2003), who proposed the existence of several fronts in a profile, and possibly arose from the contribution of the water table or laterally flowing solutions. This was accompanied by a preservation of the sedimentologic structures such as cross beds at depth, while the kaolinites experienced dissolution crystallization processes, such as in a saprolite horizon. The influence

498 of the topsoil weathering conditions may have also impacted levels as deep as P1-350, which
499 is described in the field as a sedimentary level and which is also younger than the underlying
500 level (Table 1). Thus, such a level might contain a mixture of inherited and neoformed clays.
501 The occurrence of coexisting generations of kaolinite (i.e., populations with known ages of
502 formation) in the same level was discussed for transition horizons of laterites from the region
503 of Manaus by Balan et al. (2005).

504 The EPR spectra of structural iron between the soil and sediment levels are very
505 similar, suggesting similar conditions of formation, as if a common supergene geochemical
506 process triggered the kaolinite evolution. In addition, in the sediment samples, there is a rough
507 increase in age as a function of the clay content as estimated from the Al_2O_3 concentration
508 (Figure SI 7). This suggests that the system was more stable in clay-rich levels and more open
509 and susceptible to dissolution-recrystallization in the sediments richer in sand (although
510 dissolution of quartz in the most weathered levels may also have occurred). This would
511 indicate that the environmental conditions, i.e., water drainage (infiltration or influence of a
512 water table), were conducive to the recrystallization of kaolinite. This is an argument in favor
513 of an authigenic origin of kaolinite, in line with the previous observations on the weathered
514 Alter do Chao sediments in the Manaus region by Balan et al. (2005), although very well-
515 ordered kaolinite occurred in this material. In addition, some early diagenesis of kaolin
516 sediment may have occurred soon after deposition.

517 To proceed further in the discussion, data are presented as a paleodose/dose-rate
518 diagram where the points are distributed according to isochrons (Figure 8). The two Th_{vsU} and
519 Th_{HOMO} scenarios are considered and compared to the age range proposed by Campbell et al.
520 (2006) for the deposition of the Içá Formation, according to a stratigraphic correlation with
521 the Madre de Dios Formation from Perù. The Campbell age range occurs between 2.5 and 9.5
522 Ma; thus, this domain lies (in yellow) between these two corresponding isochrons at 2.5 and

523 9.5 Ma. The soil data are located at the bottom of the diagram, consistent with their lower
524 ages. In the Th_{HOMO} scenario, it is seen that all the data from sediments, whether from artificial
525 irradiations (red) or extrapolation (green), are within the 9.5 – 2.5 Ma range proposed by
526 Campbell for the deposition of the Içá Formation, even if the error bars indicate slightly older
527 values for some ages (Figure 8 A). The Th_{HOMO} scenario strongly supports the stratigraphic
528 correlation by Campbell et al. (2006). In addition, the ages of the Içá Formation are
529 significantly younger than those of kaolinite samples from the Alter do Chao sediment at 22.2
530 - 65.3 Ma (Balan et al., 2005), as seen in Table 2. They are close to the ages of the oxisols and
531 intermediate horizons from the Manaus region (5.7-19.2 Ma, including the transition
532 horizons; Balan et al., 2005) and some samples from Sao Gabriel laterites (0.21-1.68 Ma for
533 the Ferralsol and 1.03-5.98 Ma for the Acrisol; Mathian et al., 2020). This suggests that
534 common paleoclimatic episodes are revealed in the secondary mineral record at the scale of
535 the Amazon Basin. The range of ages for the Içа samples is also consistent with the kaolinite
536 from duricrusts collected in the Barcelos or Sao Gabriel regions (Table 2 and Allard et al.,
537 2018). In addition to the sediments, data from the Quaternary (Pleistocene) period
538 corresponding to some soils are due to weathering processes that rejuvenated the kaolinites
539 and deleted the record of deposition. These data are in line with previous estimates on Içà
540 sediments by other authors, although these estimates were not supported by absolute dating
541 (Santos et al., 1974; Maia et al., 1977; Lourenço et al., 1978; Latrubesse et al., 1994; Rossetti
542 et al, 2005).

543 In the second Th_{vsU} scenario, the distribution of the data is mostly preserved, except for
544 4 samples of sediments that correspond to ages old enough to lie slightly above the upper
545 limit of the range proposed by Campbell et al. (2006). This does not necessarily contradict the
546 stratigraphic correlation considering the large error associated with our age determination;
547 thus, decisive arguments are still lacking for these 4 samples. In fact, the data presented in this

548 study do not exclude that such samples may contain, at least partly, kaolinites with a detrital
549 origin predating the deposition of the sediments.
550
551 5. Conclusions
552 The EPR dating of kaolinite from regional sediments assigned to the Içá Formation
553 specifies the chronostratigraphy of the corresponding region of Amazonia. The data indicate
554 ages in the upper Miocene–Pleistocene period, which encompasses the estimates provided so
555 far in the literature by several authors. In addition, this supports the correlation with the
556 sedimentary Madre de Dios Formation in Perù. To comprehend the scope of the presented
557 chronological data, the key issues are the distribution of thorium at the microscopic scale and
558 the determination of whether the origin of the kaolinite is authigenic (formation *in situ*),
559 detrital (inheritance from older laterites), or a mixture of the two. From the crystal chemistry
560 data, related scenarios are proposed that allow us to calculate the ages of formation for
561 kaolinite. These data suggest that some sediments are relictual in the middle of the profiles,
562 whereas the rejuvenation of kaolinite is evidenced both in the uppermost soils and at depth.
563 The proposed approach appears to be appropriate for ancient kaolinitic sediments where
564 diagenesis undoubtedly took place or where the possible lifetime in preexisting soils prior to
565 erosion and deposition in the sedimentary basin was significantly short compared to the
566 lifetime of the clay in the sediments.
567 Acknowledgments: This study was supported by the CAPES COFECUB and
568 PICS/CNRS programs. Ibtissem Boukais (IMPMC) is acknowledged regarding the fission
569 track counting. Madeleine Selo is thanked for discussion on the induced fission track
570 methodology.
571
572

573

574 References

575 Aitken M.J., 1985. Thermoluminescence dating. Studies in archaeological science. Academic
576 press, London.

577 Allard, T., Muller, JP., Dran, J.C., Menager, M.T., 1994. Radiation-induced paramagnetic
578 defects in natural kaolinites : alpha dosimetry with ion beam irradiation. Phys. Chem.
579 Miner. 21, 85-96

580 Allard, T. and Muller, J.P., 1998. Kaolinite as an in situ dosimeter for past radionuclide
581 migration at the earth's surface. Appl. Geochem., 13, 6, 751-765.

582 Allard, T., Balan, E., Calas, G., Fourdrin, C., Morichon, E., Sorieul, S., 2012. Radiation-
583 induced defects in clay minerals: A review. Nuclear Instruments and Methods in
584 Physics Research Section B: Beam Interactions with Materials and Atoms, 277, 0,
585 112-120.

586 Allard, T., Gautheron, C., Bressan-Riffel, S., Balan, E., Fernandes Soares, B., Pinna-Jamme,
587 R., Derycke, A., Morin, G., Taitson Bueno, G., do Nascimento, N., 2018. Combined
588 dating of goethites and kaolinites from ferruginous duricrusts. Deciphering the Late
589 Neogene erosion history of Central Amazonia. Chem. Geol. 479, 136-150.

590 Balan,, E., Allard, T., Boizot, B., Morin, G. and Muller, J.P., 1999. Structural Fe^{3+} in natural
591 kaolinites: new insights from electron paramagnetic resonance spectra fitting at X and
592 Q-band frequencies, Clays Clay Miner., 47, 605-616.

593 Balan, E., Neuville, D.R., Trocellier, P., Fritsch, E., Muller, J.P., Calas, G., 2001.
594 Metamictization and chemical durability of detrital zircon. Amer. Miner. 86, 9, 1025-
595 1033.

596 Balan, E., Allard, T., Fritsch, E., Selo, M., Falguères, C., Chabaux, F., Pierret, M.C. and Calas,
597 G., 2005. Formation and evolution of lateritic profiles in the middle Amazon Basin:

598 Insights from radiation-induced defects in kaolinite. Geochim. Cosmochim. Acta, 69,
599 9, 2193-2204.
600 Balan, E., Fritsch, E., Allard, T., Calas, G., 2007. Inheritance versus neoformation of kaolinite
601 during lateritic soil formation : a case study in the middle Amazon Basin. Clays Clay
602 Miner., 55, 253-259.
603 Braun, J.J., Pagel, M., Herbillon, A. , Rosin, C., 1993. Mobilization and redistribution of
604 REEs and thorium in a syenitic lateritic profile: a mass balance study. Geochim.
605 Cosmochim. Acta, 57, 4419-4434.
606 Bruno, R.D., da Rocha, H.R., de Freitas, H.C., Goulden, M.L., Miller, S. 2006. Soil moisture
607 dynamics in an eastern Amazonian tropical forest. Hydrol. Proc., 20, 2477-2489.
608 Campbell, K.E., 2001. Cenozoic chronostratigraphy of the southwestern Amazon Basin.
609 Geology, 595-598.
610 Campbell, K.E., Frailey, C.D., Romero-Pittman, L., 2006. The Pan-Amazonian Ucayali
611 Peneplain, late Neogene sedimentation in Amazonia, and the birth of the modern
612 Amazon River system. Pal. Pal. Pal., 239, 166–219.
613 Campbell, K.E., 2010. Late Miocene onset of the Amazon River and the Amazon deep-sea
614 fan: Evidence from the Foz do Amazonas Basin: comment. Geology. E212. doi:
615 10.1130/G30633C.1
616 Chabaux, F., Dequincey, O., Lévèque, J.J., Leprun, J.C., Clauer, N., Riotte, J., Paquet, H.,
617 2003. Tracing and dating recent chemical transfers in weathering profiles by trace-
618 element geochemistry and ^{238}U–^{234}U–^{230}Th disequilibria: the example of the Kaya
619 lateritic toposequence (Burkina-Faso). C-R. Acad. Sci., Geoscience, 335, 1219–1231.
620 Clozel, B., Allard, T. and Muller, J.-P., 1994. Nature and stability of radiation induced defects
621 in natural kaolinites: New results and a reappraisal of published works. Clays clay
622 miner., 46, 657-666.

623 CPRM (2010). Mapa geológico do Brasil. Serv. Geol, Brasil, Brasília ([Online] URL: http://
624 geobank.sa.cprm.gov.br (accessed December 2010)).
625 Da Costa, M.L., Souza, D. J. L., Angélica, R.S., 2009. The contribution of lateritization
626 processes to the formation of the kaolin deposits from eastern Amazon. J.South Amer.
627 Earth Sci.,, 27, 219-234.
628 Da Costa, M.L., da Silva Cruz, G., de Almeida, H.D.F., Poellmann, H., 2014. On the geology,
629 mineralogy and geochemistry of the bauxite-bearing regolith in the lower Amazon
630 Basin: Evidence of genetic relationships. J. Geochem. Explor., 146, 58-74.
631 De Almeida, R.P., Galeazzi, C.P., Freitas, B.T., Janikian, L., Ianniruberto, M., Marconato, A.,
632 2016. Large barchanoid dunes in the Amazon river and the rock record : implications
633 for interpreting large river systems. Eart Planet Sci. Lett.,, 454, 92-102.
634 Duval, M. (2012) Dose response curve of the ESR signal of the Aluminum center in quartz
635 grains extracted from sediment. Ancient TL, 30, 2, 41-49.
636 Figueiredo,, J., Hoorn, C., van der Ven, P., Soares, E., 2009. Late Miocene onset of the
637 Amazon river and the Amazon deep-sea fan: evidence from the Foz do Amazonas
638 Basin. Geology, 37, 7, 619-622.
639 Fritsch, E., Balan, E., do Nascimento, N.R., Allard, T., Bardy, M., Bueno, G., Derenne, S.,
640 Melfi, A.J., 2011. Deciphering the weathering processes using environmental
641 mineralogy and geochemistry: Towards an integrated model of laterite and podzol
642 genesis in the Upper Amazon Basin. Comptes Rendus Acad. Sci. Geoscience. 343,, 2–
643 3, 188-198.
644 Hennig, G.J. and Grün, R., 1983. ESR dating in quaternary geology. Quat. Sci. Rev. 2, 157-
645 238.
646 Hinckley, D.N., 1963. Variability in “Crystallinity” values among the kaolin deposits of the
647 coastal plain of Georgia and South Carolina. Clay Clay Miner. Monogr. 13, 229–235.

Horbe, A. M. C., Motta, M. B., de Almeida, C. M., Dantas, E. L., Cruz Vieira, L., 2013. Provenance of Pliocene and recent sedimentary deposits in western Amazônia, Brazil: Consequences for the paleodrainage of the Solimões-Amazonas River. Sedim. Geol., 296, 9-20.

Hoorn, C., Vonhof, H., 2006. Neogene Amazonia : Introduction to the special issue. J. South Amer. Earth Sci., 21, 1-4.

Hoorn,, C., Wesselingh, F. P., ter Steege, H, Bermudez, M. A., Mora Sevink, J., Sanmartín, I., Sanchez-Meseguer, A., Anderson, C. L., Figueiredo, P., Jaramillo, C., Riff, D., Negri, F. R., Hooghiemstra, H., Lundberg, J., Stadler, T., Särkinen, T., Antonelli, A., 2010. Amazonia Through Time: Andean uplift, climate change, landscape evolution, and biodiversity. Science, 330, 927-931.

Hoorn, C., Wesselingh, F. P., 2010. Amazonia: landscape and species evolution. A look into the past. Wiley-Blackwell. 447 p.

Ikeya, M., 1993. New applications of electron spin resonance. Dating, dosimetry and microscopy. Applied Magnetic Resonance. World Scientific, Singapore.

Latrubesse, E.M., Rancy, A., Ramonell, C.G., Souza Flho, J.P., 1994. A Formação Solimões: uma formação do Mio-Plioceno da Amazônia sul-ocidental. In: Simpósio de Geologia da Amazônia, 4, 1994. Boletim de Resumos Expandidos, Belém, Sociedade Brasileira de Geologia-Núcleo Norte, 204-205.

Latrubesse, E.M., Silva, S.A.F., Cazzuol, M., Absy, M.L., 2007. Late Miocene continental sedimentation in southwestern Amazonia and its regional significance: biotic and geological evidence. Journal of South American Earth Sciences, 23, 61–80.

Lourenço, R.S.; Montalvao, R.M.G.; Pinheiro, S.S.; Fernandes, P.E.C.A.; Pereira, E.R.; Fernandes, C.A.C.; Teixeira, W. Geológica. In: PROJETO RADAMBRASIL. Folha SA 20. Rio de Janeiro, DNPM 1978. v.18, I, 19-164 p.

Lucas, Y., Nahon, D., Cornu, S., Eyrolles, F., 1996. Genèse et fonctionnement des sols en

674 milieu equatorial. C.R. Acad. Sci. Paris, t. 322, série II a, 1-16.
675 Lucas, Y., Montes, C.R., Mounier, S., Cazalet, M., Loustau, M., Ishida, D., Achard, R.,
676 Garnier, C., Coulomb, B., Melfi, A.J., 2012. Biogeochemistry of an Amazonian
677 podzol-ferralsol soil system with white kaolin. Biogeosciences, 9, 9, 3705–3720.
678 Maia, R.G., Godoy, H.K., Yamaguti, H.S., Moura, P.A., Costa, F.S., 1977. Projeto carvão no
679 Alto Amazonas. Final report. CPRM, Rio de Janeiro.
680 Mathian, M., Aufort, J., Braun, J.J., Riotte, J., Selo, M., Balan, E., Fritsch, E., Bhattacharya,
681 S., Allard, T., 2019. Unraveling weathering episodes in Tertiary regoliths by kaolinite
682 dating (Western Ghats, India). Gondwana Research**,** 69, 89-105.
683 Mathian, M., Taitson Bueno, T. G., Balan, E., Fritsch, E., do Nascimento, N.R., Selo, M.,
684 Allard, T., 2020. Kaolinite dating from Acrisol and Ferralsol: a new key to
685 understanding the landscape evolution in NW Amazonia (Brazil) Geoderma (in press).
686 Mehra, O.P., Jackson, M.L., 1960. Iron oxide removal from soils and clays by dithionite-
687 citrate buffered with sodium bicarbonate. Clays Clay Miner. 7, 317-327.
688 Montes, C.R., Lucas, Y., Melfi, A.J., Ishida, D.A., 2007. Systèmes sols ferrallitiques-podzols
689 et genèse des kaolins. C.R. Geoscience 339, 50-56.
690 Morichon, E., Allard, T., Beaufort, D., Patrier, P., 2008. Evidence of native radiation-
691 induced paramagnetic defects in natural illites from unconformity-type uranium
692 deposits. Phys. Chem. Miner. 35, 339-346.
693 Muller, J-P., Calas, G., 1989. Tracing Kaolinites through Their Defect Centers : Kaolinite
694 Paragenesis in a Laterite (Cameroon). Econ. Geol., 84, 1989, 694-707.
695 Muller, J-P., Clozel, B., Ildefonse, P., Calas,, G., 1992. Radiation-induced defects in kaolinites:
696 indirect assessment of radionuclide migration in the geosphere. Appl. Geochem. Suppl.
697 Issue No. I, 205-216.

698 Muller, J-P., Calas, G., 1993. Genetic Significance of Paramagnetic Centers in Kaolinites, in
699 Murray, H.H., Bundy, W.M., Harvey C.C. (Eds) Kaolin genesis and utilization, CMS
700 special publication, 1-13.
701 Passos, M.S., Soares, E.A.A., Tatumi, S.H., Yee, M., Mittani, J.C.R., Hayakawa, E.H.,
702 Salazar, C.A., 2020. Pleistocene-Holocene sedimentary deposits of the Solimões-
703 Amazonas fluvial system, Western Amazonia, J. South Amer. Earth Sci.
704 https://doi.org/10.1016/j.jsames.2019.102455 .
705 Price, P.B., Walker, R.M., 1963. A simple method for measuring low uranium concentrations
706 in natural crystals. Appl. Phys. Lett., 2, 23-25.
707 Projeto Radam (or Radam Brazil), 1972–78. Levantamento de Recursos Naturais. Ministerio
708 das Minas e Energia, Departamento Nacional da Producxa o Mineral, Rio de Janeiro,
709 Brazil.
710 Reis, N.J., Ferreira, A.L., Riker, S.L., Almeida, M.E. (Eds.), 2006. Geologia e recursos
711 minerais do estado do Amazonas. Manaus: CPRM/CIAMA. Escala 1:1.000.000.
712 [Texto explicativo]. 148 p. CD-ROM.
713 Rossetti, D.F., Toledo, P.M., Góes, A.M., 2005. New geological framework for Western
714 Amazonia (Brazil) and implications for biogeography and evolution. Quat. Res., 63,
715 78–89.
716 Rossetti, D. F., Cohen, M. C. L. , Tatumi, S. H., Sawakuchi, A. O., Cremon, E. H., Mittani, J.
717 C. R., Bertani, T. C., Munita, C. J. A. S., Tudela, D. R. G., Yee Moya, M., G., 2015.
718 Mid-Late Pleistocene OSL chronology in western Amazonia and implications for the
719 transcontinental Amazon pathway. Sedim. Geol., 330, 1-15.
720 Santos, J.O.S., Moreira, A.S., Pessoa, M.R., Oliveira, J.R.; Malouf, R.F., Veiga Jr., J.P. &
721 Nascimento, J.O., 1974. Projeto Norte da Amazônia, Domínio Baixo Rio Negro;
722 Geologia da Folha NA.20-Z. Relatório Final, Manaus, DNPM/CPRM, v.III ASélo, M.,

1983. La fission nucléaire et sa signification en Géochronologie, Paleothermométrie et Géochimie. Applications à l'étude particulière des basaltes océaniques. Unpublished phD Thesis, University Paris VI.

Sousa, D. J. L., Varajao, A.F.D.C., Yvon, J., da Costa, G.M., 2007. Mineralogical, micromorphological and geochemical evolution of the kaolin facies deposit from the Capim region (northern Brazil). Clay Miner. 42, 69-87.

de Souza, E.L., Galvão, P. H. F., Pinheiro, C.S.S., Baessa, M.P.M., Demétrio, J.G.A., Brito, W.R.R., 2013. Sintese da hidrogeologia nas bacias sedimentares do Amazonas e do Solimões: Sistemas aquiferso Içá-Solimões e Alter do Chão. Geol. USP, Sér. Cient. São Paulo, 13, 1, 107-117.

Yokoyama, Y. and Nguyen, H. V., 1980. Direct non-destructive dating of marine sediments, manganese nodules and corals by high-resolution gamma-ray spectrometry, in. Goldberg, E. D., Horibe, Y., Saruhash,i K. (eds), Isotope Marine Chemistry,. pp. 259–289. Uchida Rokakuho Pub. Co. Ltd, Tokyo.

Ziegler, J.F., Ziegler, M.D., Biersack, J.P., 2010. SRIM - The stopping and range of ions in matter (2010) Nucl. Inst. Meth. Phys. Res. B. 268, 11-12, 1818-1823.

740 Figure captions

741 Figure 1: Maps of the studied region. (A) Location of the study area (white rectangle)
742 in Amazonia (white delineated area). (B) Geological map of the studied region in Amazonia,
743 showing the extent of the Içá Formation. See Reis et al. (2006) for the legend of other
744 geological formations. (C) Location of the selected sites in the study area, region of Barcelos.

745 Figure 2: Studied profiles and location of the selected samples.

746 Figure 3: Plot of the uranium and thorium concentrations in all raw samples (before
747 selection according to the vanadyl content). The good correlation for most samples suggests
748 that these elements are located in the same clay size fraction or hosted in common bearing
749 minerals. Gray squares correspond to laterites and open circles to sediments as recognized in
750 the field.

751 Figure 4: Optical microscopy in natural light: thin sections of P2-530 (A) and P4-1000
752 (B) and induced fission track mapping of P4-1000 showing both dispersed tracks and an
753 "urchin"-like concentration (C). Dominant quartz grains (Qz) are embedded in a beige clayey
754 matrix (Ma) with some patches of rusty iron oxides (FeOx). SEM of selected samples: in
755 secondary electrons (D) and backscattered electrons (E) on P1-760 showing dominant small-
756 sized kaolinites and minor booklets (Bk). Minor flat booklets dispersed in small kaolinites in
757 P4-1000, secondary electrons (F).

758 Figure 5: Total EPR spectra of kaolinite groups of local crystalline disorder
759 determined from the signal of structural Fe^{3+} (according to the relative amplitudes of the so-
760 called Fe(II) and Fe(I) signals). The amplitude of the spectra (in arbitrary units) is scaled for
761 the diagram.

762 Figure 6: Normalized EPR spectra in the g = 2 region. Notice the hyperfine structure
763 of vanadyl compared to VO^{2+}-rich reference dickite from Mexico (Dimex) and the RID signal
764 compared to the GB1 kaolinite reference. Central resonances of the vanadyl spectrum overlap

765 the components of the RIDs in kaolinite. The isolated component at g= 1.881 is used to
766 determine the interference from the vanadyl signal.

767 Figure 7: Dosimetry with He^+ ions. Experimental data are fitted, when appropriate, by
768 simple exponential or exponential + linear functions. The paleodose is the extrapolation of the
769 dosimetry curve to the X axis.

770 Figure 8: Diagrams of paleodose versus dose rate for sediments (full squares) and soils
771 (half-full squares) located according to selected isochrones (dotted lines) and by comparison
772 to the Miocene-Pliocene range of ages (2.5 – 9.5 Ma interval in yellow) proposed by
773 Campbell et al. (2006) for the Içà Formation. Red represents age determination from artificial
774 irradiation, and green represents extrapolation. Two scenarios of age calculation are
775 considered, where the distribution of thorium in the matrix is a critical parameter: one for a
776 homogeneous distribution (A) and one for a distribution similar to that of uranium (B).
777 Irrespective of the considered model, most data are consistent with the stratigraphic
778 correlation of Campbell et al. (2006), except a few with higher ages in the second scenario
779 that could possibly correspond at least partly to detrital kaolinite generations.

780

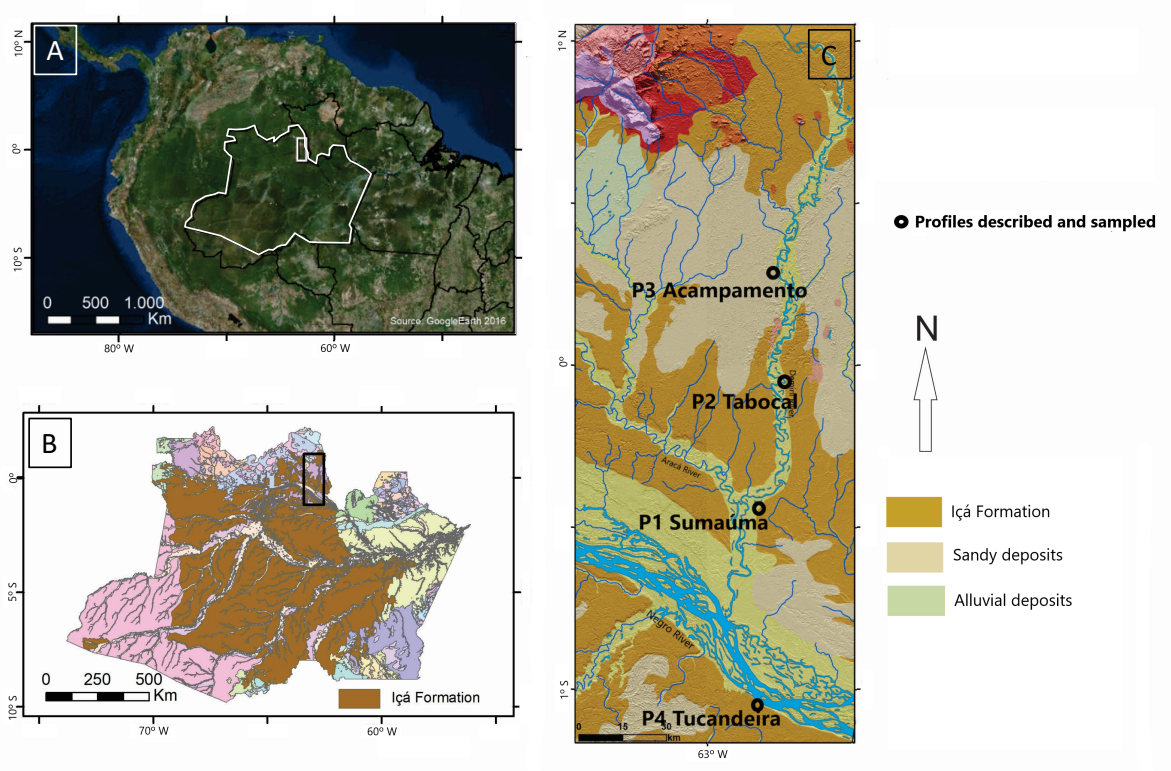

781

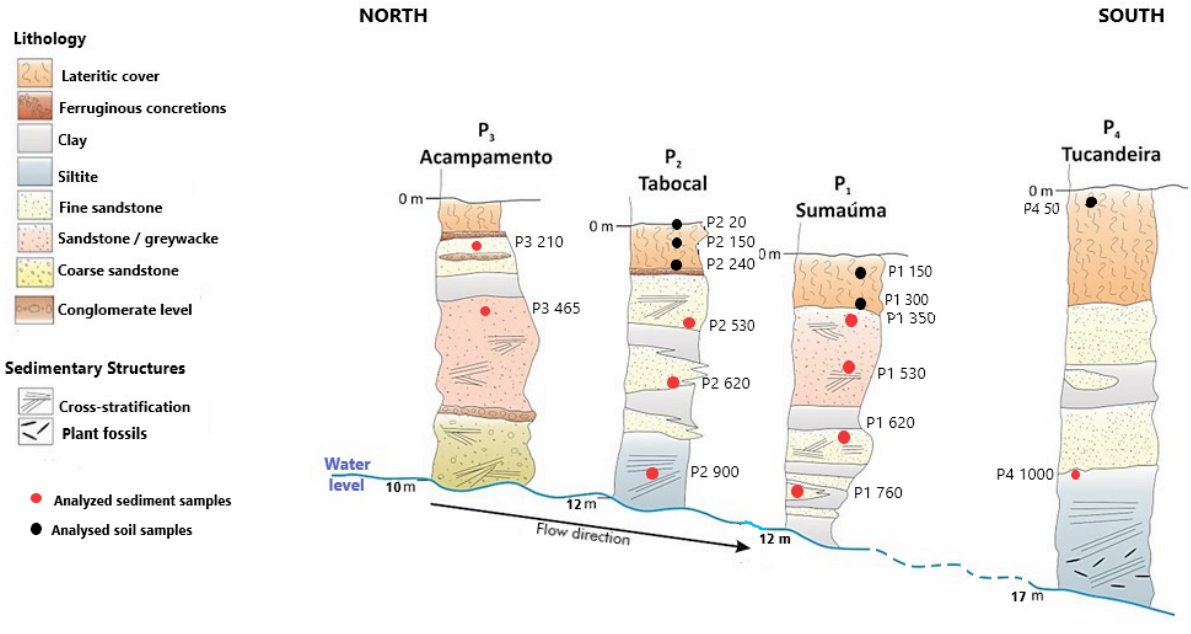

Figure 2

782

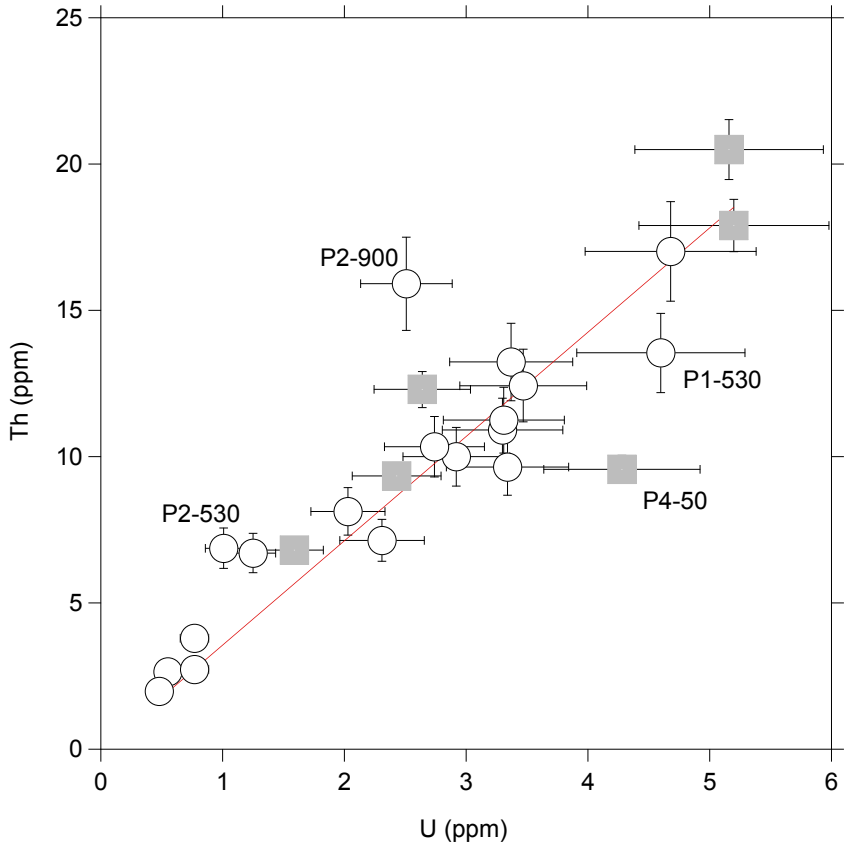

Figure 3

783

784

785

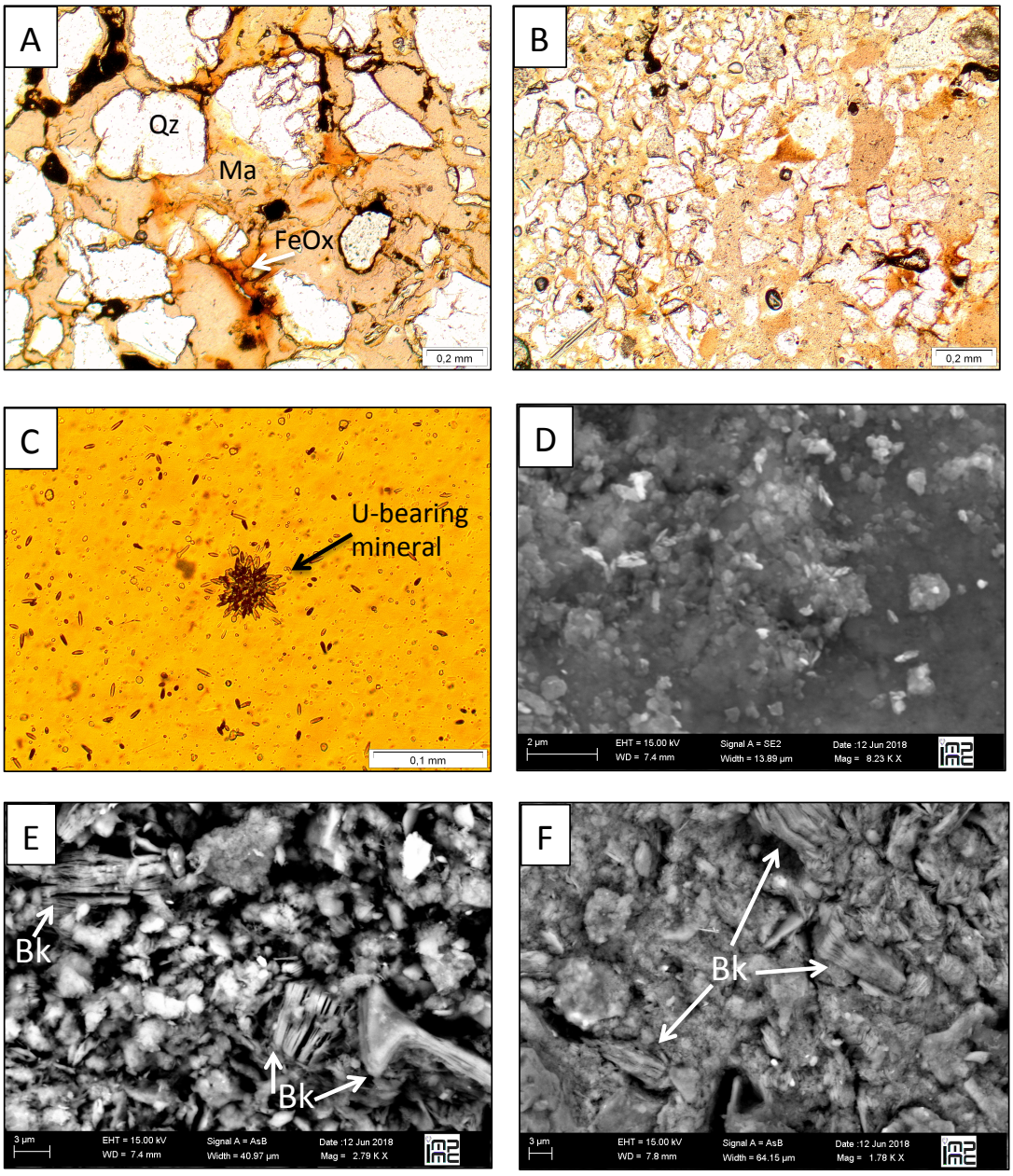

Figure 4

786

787

788

789

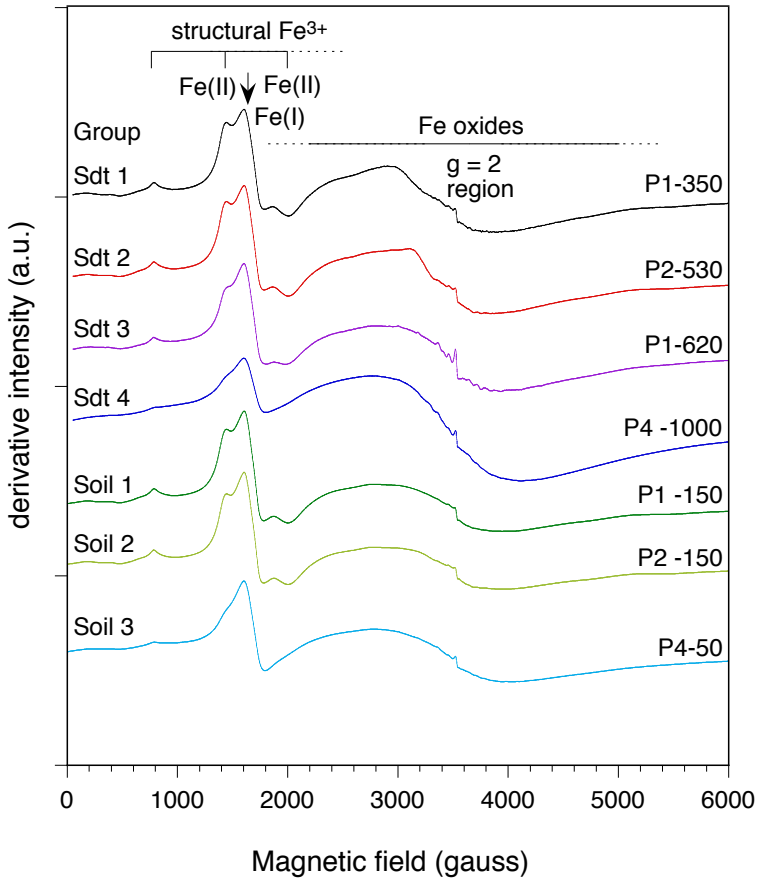

Figure 5

790

791

792

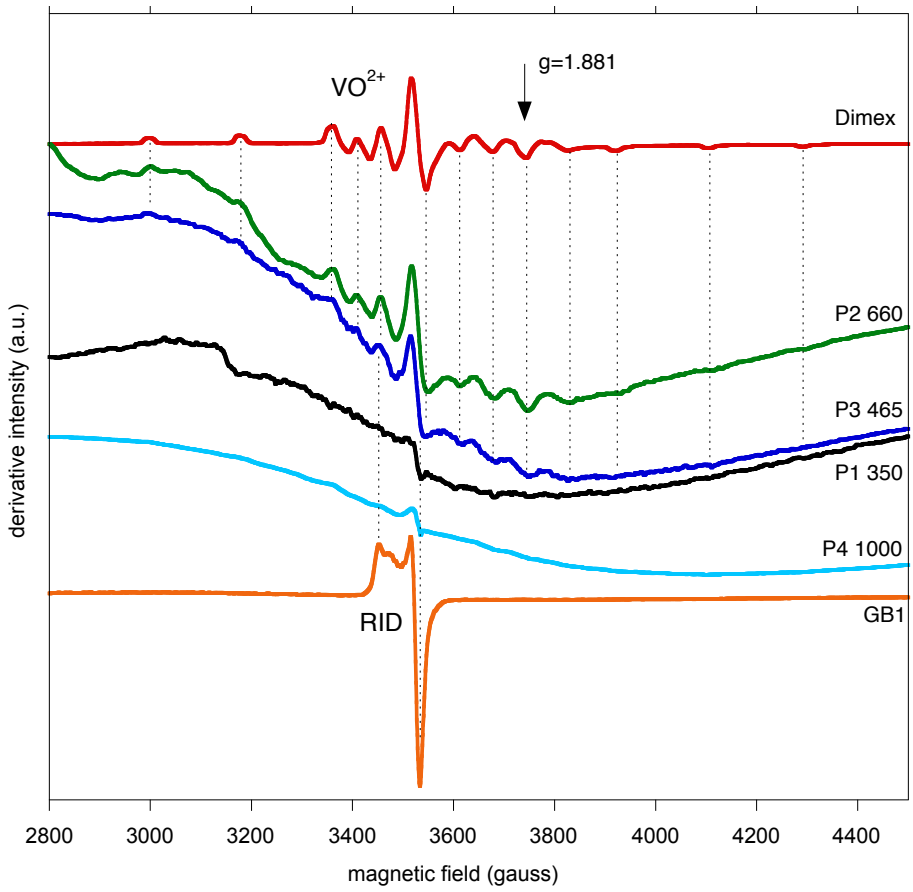
VO2+
g=1.881
Dimex
P2 660
P3 465
P1 350
P4 1000
GB1
RID
derivative intensity (a.u.)
2800
3000
3200
3400
3600
3800
4000
4200
4400
magnetic field (gauss)

Figure 6

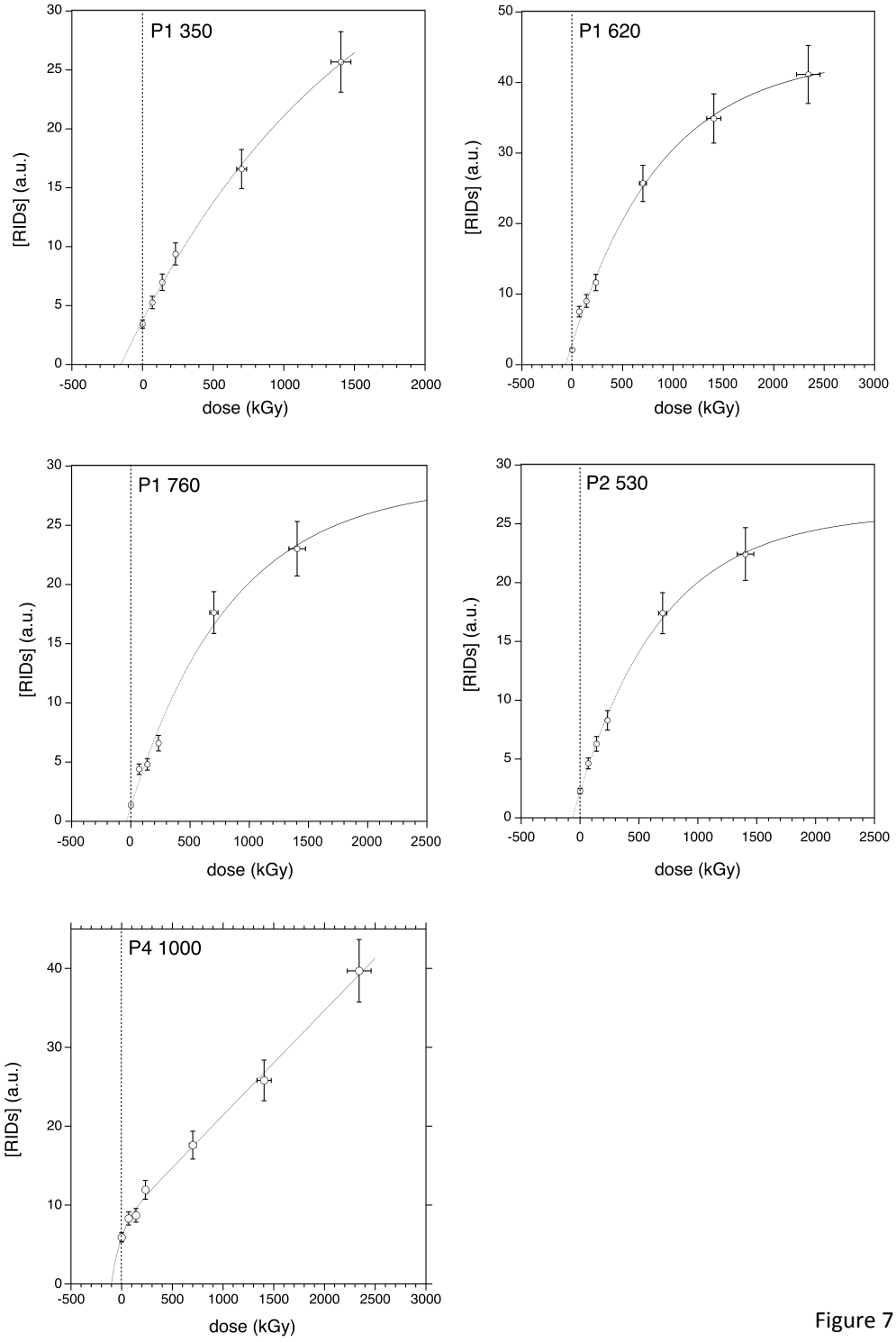

Figure 7

796

797

798

799

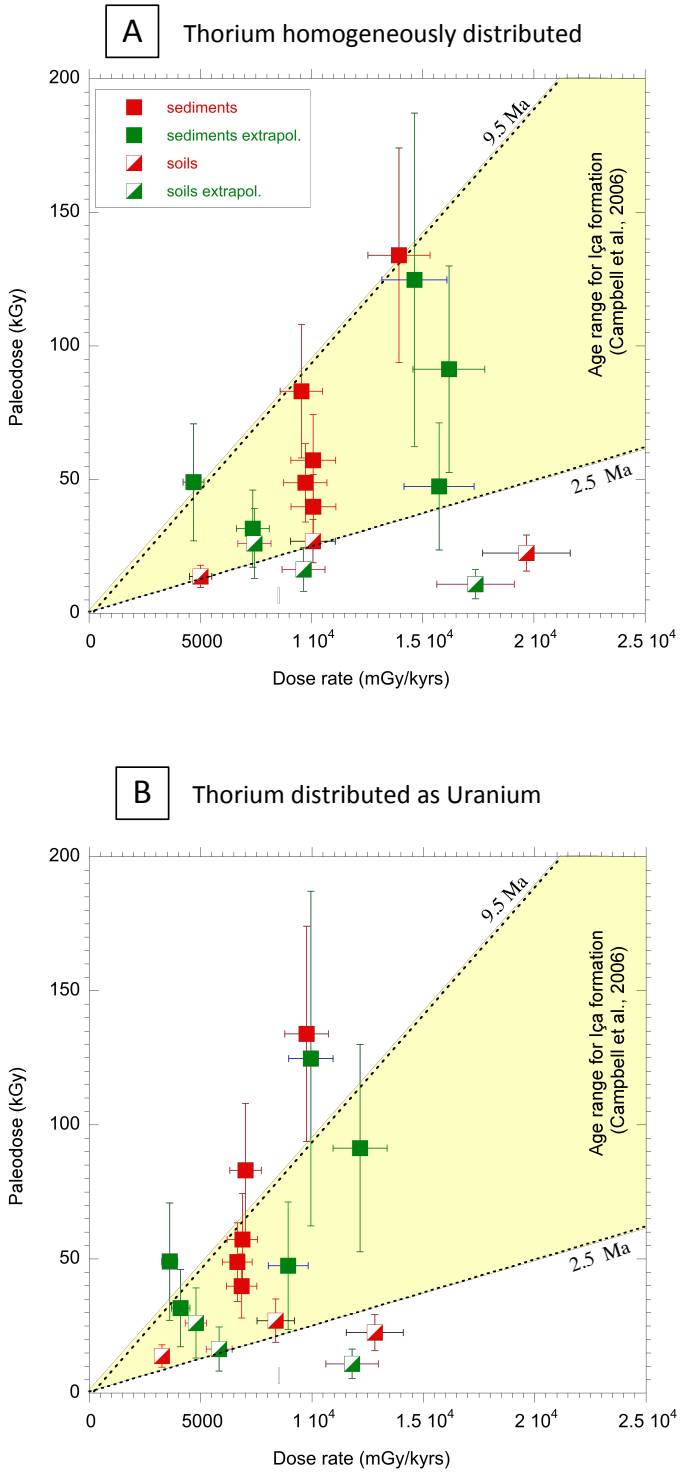

Figure 8

800

801

802

803

804

Sample	Material	Group [a]	% RID[b]	[RID] cor[c] (a.u.)	[U] (ppm)	[Th] (ppm)	[K] (%)	[Al_2O_3] (%)[d]	Rn Budget (±%)[e]	U in matrix (%)[f]	Paleodose (kGy)[g]
P1-150* [FT]	soil	Soil 1	52.4	1.31	5.16	20.50	0.09	34.31	+20	36.8	22.55*
P1-300	soil	Soil 2	45.44	0.80	5.20	17.90	0.11	30.80	+20**	36.8	10.92
P1-350* [FT]	sdt	Sdt 1	100	3.87	3.34	9.65	0.07	11.34	-9.0**	36.8	57.72*
P1-530	sdt	Sdt 2	64	3.44	4.6	13.55	0.09	15.72	-9.0	38.15	124.73
P1-620*	sdt	Sdt 3	37	2.12	2.92	10.00	0.25	11.40	-9.0	38.15	39.94
P1-760* [FT]	sdt	Sdt 1	28	1.37	2.74	10.34	0.15	9.41	-9.0	39.5	48.85*
P2-20	soil	Soil 2	73.23	1.72	2.43	9.34	0.00	13.96	+35	30.0	26.13
P2-150	soil	Soil 2	64.5	0.99	2.64	12.30	0.03	20.09	+35	30.0	16.86
P2-240*	soil	Soil 2	30.55	0.99	1.59	6.81	0.03	6.74	+35**	30.0	13.83*
P2-530* [FT]	sdt	Sdt 2	59	2.29	1.01	6.87	0.04	8.38	+12.5**	57.9	83.05*
P2-660	sdt	Sdt 1	26	2.04	0.77	3.80	0.01	2.79	+12.5	57.9	27.18
-	-	-	-	-	-	-	-	-	-	-	70.93
P2-900	sdt	Sdt 1	70	3.63	2.51	15.91	0.11	24.96	+12.5	57.9	52.73
-	-	-	-	-	-	-	-	-	-	-	129.93
P3-210	sdt	Sdt 1	49	1.34	2.03	8.13	0.03	6.67	+5.5	26.1	17.27
-	-	-	-	-	-	-	-	-	-	-	46.11
P3-465 [FT]	sdt	Sdt 2	40	1.39	4.68	17.02	0.16	13.03	+5.5**	26.1	47.51
P4-50* [FT]	soil	Soil 3	42.8	1.52	4.28	9.57	0.15	8.60	-8.0**	40.0	27.01*
P4-1000* [FT]	sdt	Sdt 4	100	5.90	3.47	12.43	1.30	17.36	-5.7**	40.5	133.92*

805
806 Table 1 : Parameters of age determination for soil and sediment (sdt) samples (see text for assumptions on dose rate corrections)
807 derived from artificial irradiation. a: group of degree of crystalline disorder. b: RID signal proportion in the total EPR signal
808 estimated after removal of the vanadyle interference. c: concentration of RIDs corrected for vanadyle interference;. d: the con
809 Al_2O_3 is used to estimate the clay content. Kaolinite is considered as the major Al-bearing mineral in the < 2 µm fraction : a 10
810 content then corresponds to 39 % of Al_2O_3.. e: the Rn budget (relative loss of gain with respect to U) is determined by gamma
811 on samples labeled by **. f: the part of U located in the clayey matrix is determined by induced-fission track counting [FT].
812 paleodose are derived from the dosimetry curve fitting (*= irradiated samples) or extrapolated for samples of the same group. In
813 possible models (related to P1-350; and P1-760) were used to illustrate the variation of extrapolated ages when different possibl
814 considered. Thus, two values of paleodoses are given for samples P2-660, P2-900, P3-210 that all belong to the first group. h
815 dose rate and ages according to : Radon gain or loss, 20 % average water content, U distribution among U-bearing minerals an
816 geometry effect of the quartz/matrix bodies. h: value for Th distribution similar to that of U; i: Th homogeneous distribution in t
817
818
819
820
821
822
823
824
825
826
827

Region in Amazonia	Material	Age range (Ma)	Reference
Manaus	Weathered Alter do Chao (Cretaceous) sediments	22.2 - 65.3	Balan et al. (2005)
-	Soil + transition	5.7 - 19.2	-
Santa Isabel	Duricrust within soil	1.7- 4.0	Allard et al. (2018)
Sao Gabriel	Duricrust within soil	7.2 - 16.7	-
Sao Gabriel	Soil (Ferralsol) + saprolite	0.21 - 1.68	Mathian et al. (2020)
-	Soil (Acrisol) + saprolite	1.03 - 5.98	-
Barcelos	Içà sediments	2.3 – 19.6	This study
-	Soil	0.6 – 5.0	-

Table 2 :Summary of kaolinite dating in laterites and sediments from the central and western Amazon Basin.

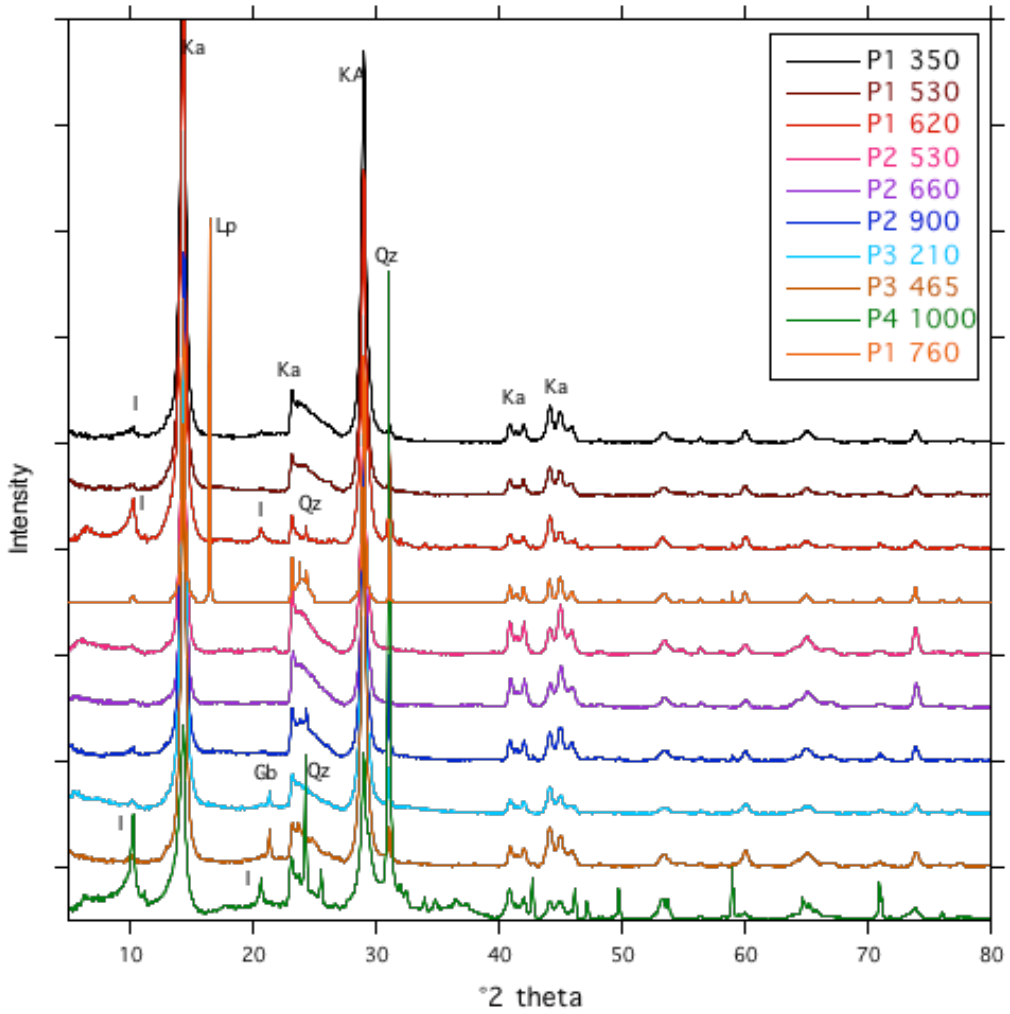

Figure SI 1 A : Powder diffractograms (baseline corrected) of studied sediments (< 5μm fraction). Ka: Kaolinite; Qz: quartz; I: Illite; Gb: Gibbsite. The kaolinite is by far the most abundant mineral.

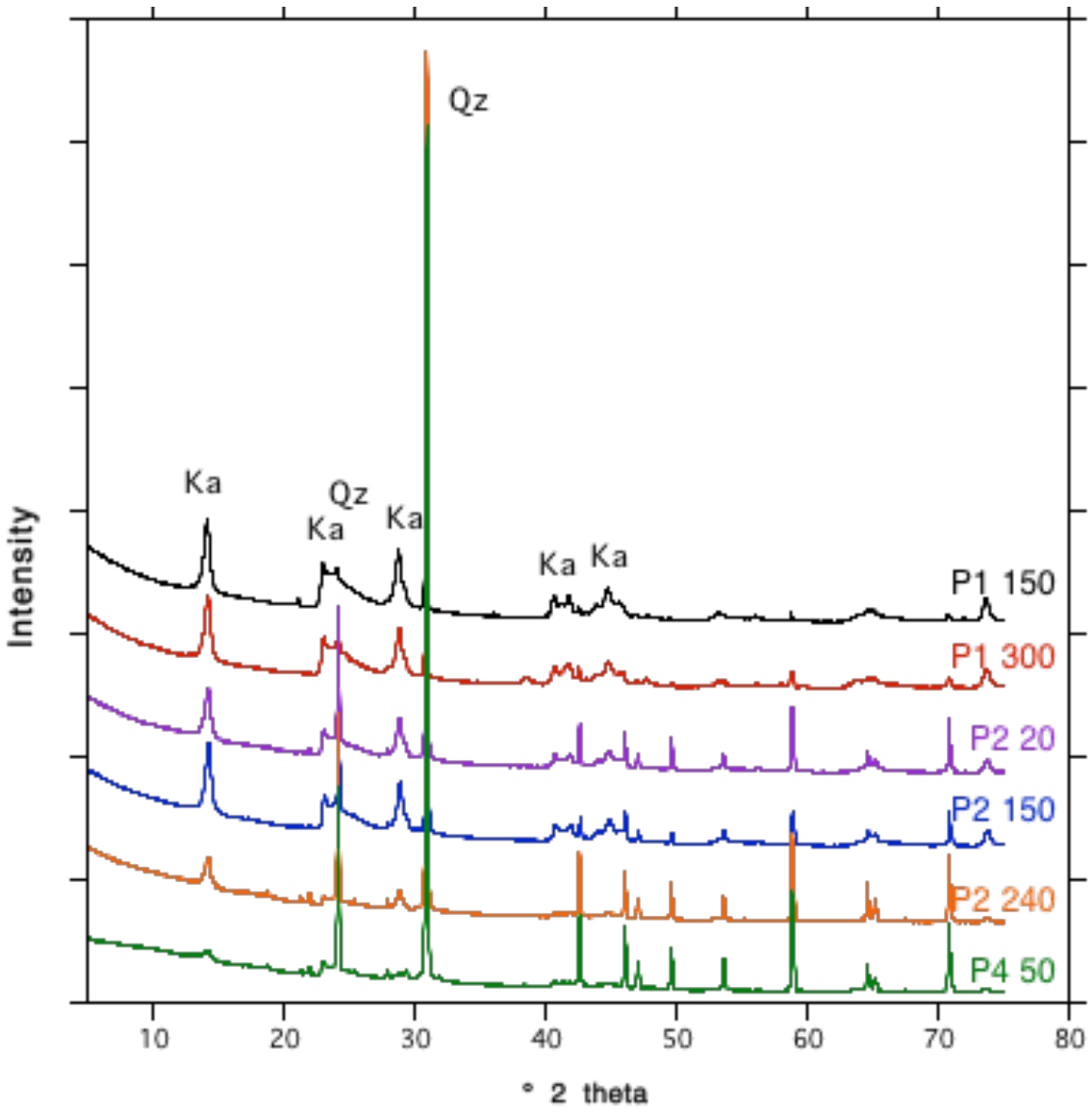

Figure SI 1 B : Powder diffractograms of studied soils (< 5μm fraction). Ka: Kaolinite; Qz: quartz; The kaolinite is the dominant secondary mineral. Quartz is dominant in the P2 and P4 samples.

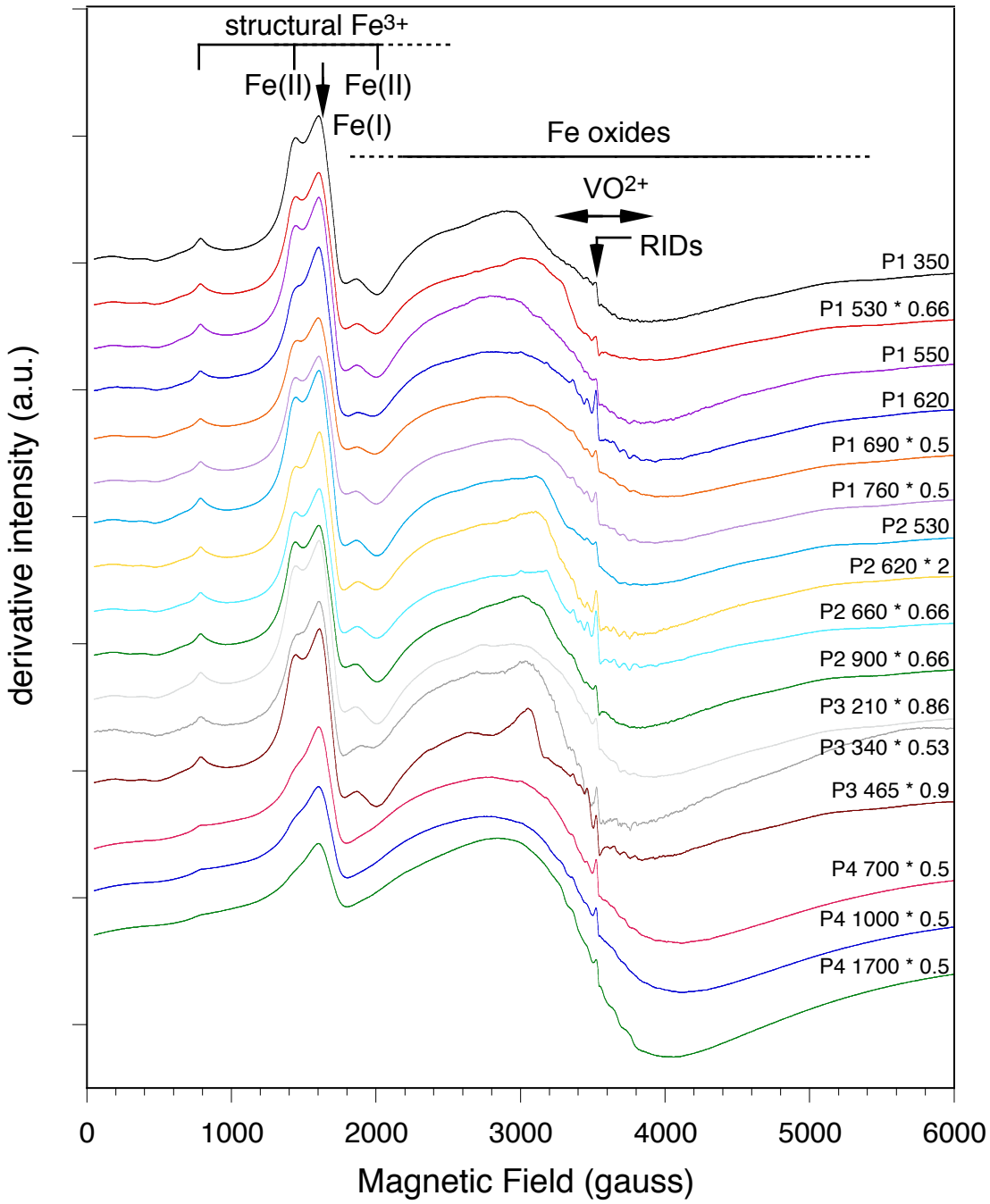

Figure SI 2A : total spectra of all sediment samples originating from the 4 profiles in the Içà formation. Regions of the spectra related to several paramagnetic species are indicated together with the factor of normalization of derivative amplitude.

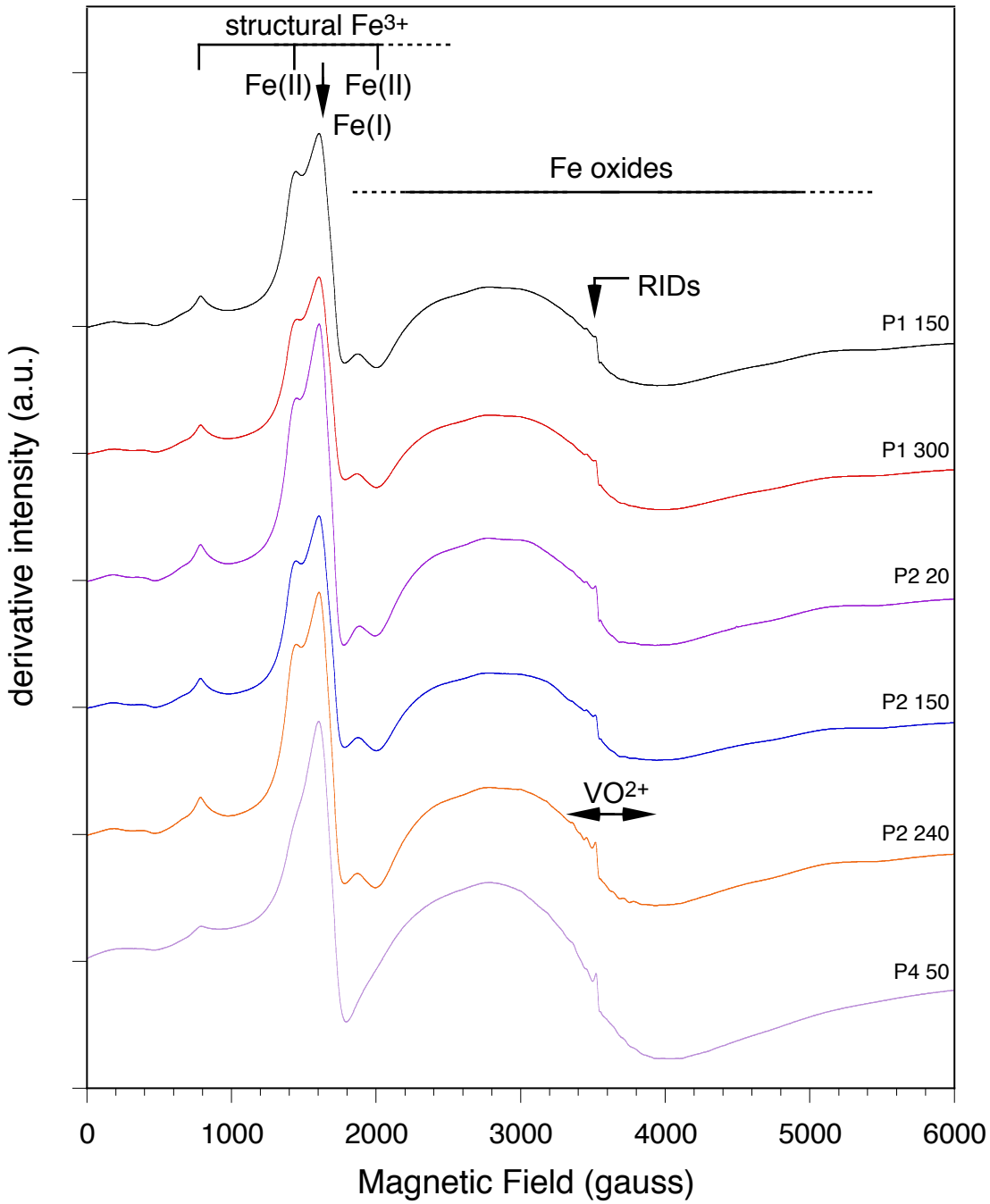

Figure SI 2B : total spectra of all soil samples originating from 3 profiles in the Içà formation. Regions of the spectra related to several paramagnetic species are indicated as in SI1A.

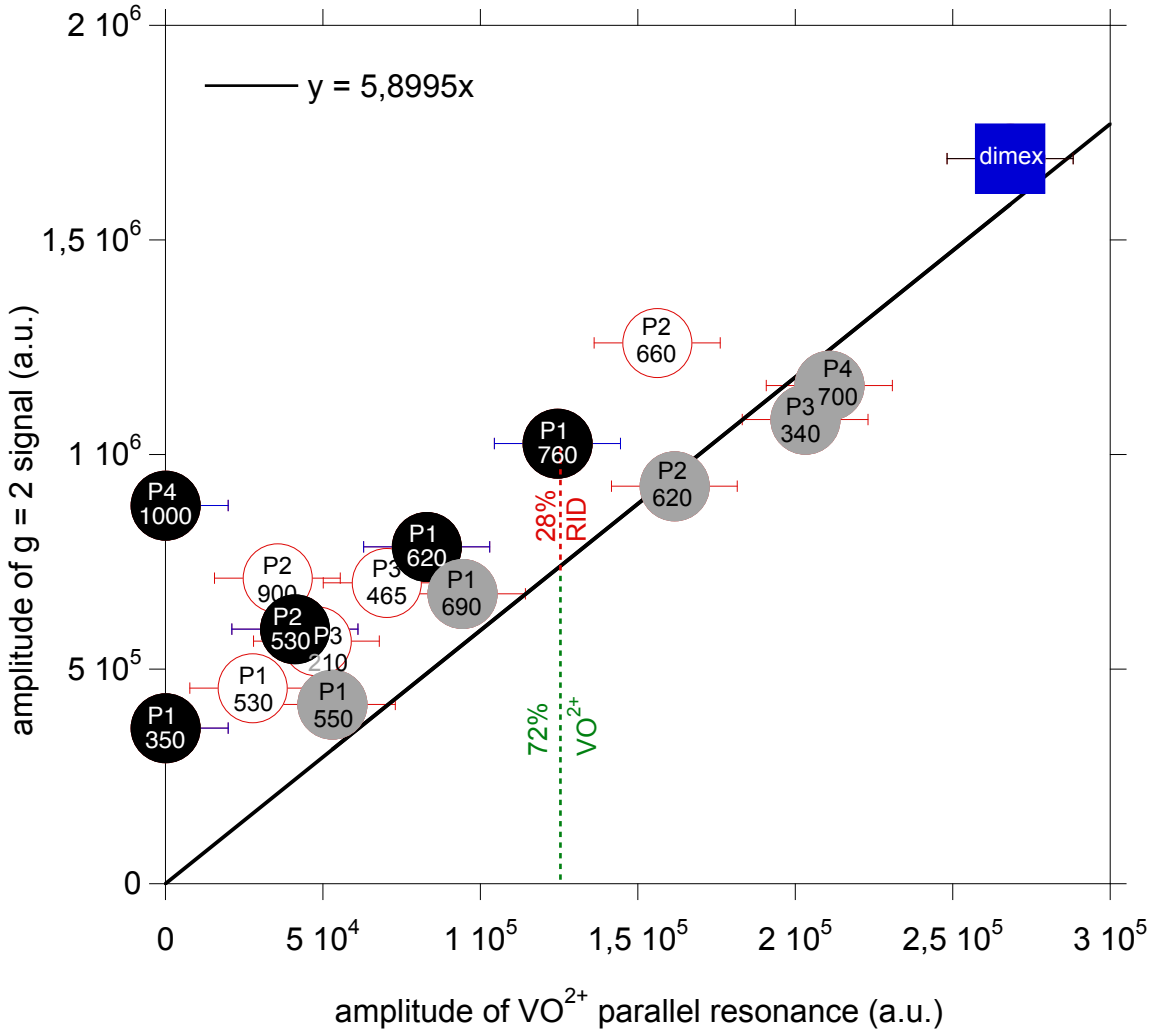

Figure SI 3 : Relative amplitude of the RID signal with respect to the interfering VO^{2+} signal for sediment samples. Both signals occur at the same magnetic field in the g=2 region. A 100 % vanadyle contribution line is defined using the vanadyl standard (Dimex) and some VO^{2+}-rich kaolinites. The procedure of measurement of RID intensity is illustrated for the P1-760 sample. Points in gray correspond to discarded samples for which the VO^{2+} signal is dominant. All data above the line contain significant amplitude ot the RIDs signal (white and black points). The black points stand for the samples selected for artificial irradiation, including two samples with no measurable vanadyl contribution (P-350, P4-1000).

Table SI 4a: concentrations of RIDs (arbitrary units) in artificial He^{+}-irradiation experiments. Data in italics correspond to aberrant points.

Fluence (ions/cm^2)	Dose (kGy)	P1-150	P1-350	P1-620	P1-760	P2-240	P2-530	P4-50	P4-1000
0	0	1.31	3.87	2.12	1.37	0.99	2.29	1.52	5.90
3e+11	70	3.79	5.26	7.52	4.4	3.95	4.63	3.80	8.30
6e+11	140	5.22	6.98	9.02	4.81	5.90	6.29	4.61	8.70
1e+12	234	6.98	9.39	11.6	6.61	7.11	8.29	5.05	11.94
3e+12	702	14.32	16.58	25.71	17.63	17.61	17.41	8.04	17.60
6e+12	1405	25.82	25.68	34.9	23.02	30.58	22.44	10.00	25.80
1e+13	2342	40.72		41.16	*35.94*	44.18	*38.89*	12.92	39.70

Table SI 4b: dosimetry parameters : [Cs] saturation (arbitrary units), λ exponential factor (kGy^{-1}), LF linear factor, if required (kGy^{-1})

Sample	[Cs]	λ	LF
P1-150	2.81	0.01835	0.0160407
P1-350	7.93	0.0087	0.0136
P1-620	41.04	0.0014	
P1-760	31.56	0.000952	
P2-240	2.91	0.0208818	0.0187
P2-530	26.16	0.0013	
P4-50	4.471	0.0141608	0.0038
P4-1000	6.96	0.0070	0.0128

SI 5: Simple model of dose rate correction in a heterogeneous sample

In a homogeneous medium, the radiation dose deposited by alpha particles emitted during the radioactive decay of uranium, referred to as D_U, is linearly related to the uranium wt. concentration [U].

We now consider the radiation dose, $D_{U,corr}$, deposited in a heterogeneous medium composed of spherical quartz grains of radius r embedded in a homogeneous kaolinite matrix. The wt. concentration of kaolinite and quartz are [kao] and [Qtz], respectively.

For a medium where uranium only occurs in the clayey fraction and is absent in quartz grains, two effects have to be considered: an increase of the U concentration in the clay matrix, due to the excluding effect of quartz, and a decrease of the deposited dose in the matrix due to the absorption of radiation by the quartz grains.

A balance of the energy deposited in the sample gives:

$M_{tot} D_U = D_{U,corr} (M_{qtz,\,irr} + M_{kao})$ (Eq. 1)

where M_{tot}, M_{kao} and $M_{qtz,irr}$ are the sample mass, the kaolinite mass and the irradiated quartz mass, respectively. Assuming that the size of the quartz grains is large with respect to the penetration depth d of alpha particles, the volume occupied by the irradiated quartz $V_{qtz,irr}$ is that of a spherical shell of thickness d: $V_{qtz,irr} = 4/3\ \pi\ r^3 - 4/3\ \pi\ (r-d)^3$

The fraction of irradiated quartz is thus: $f = V_{qtz,irr} / V_{qtz} = 1 - (1- a)^3$ with $a=d/r$,

leading to $f = a(a^2-3a+3)$

Accordingly, Eq. 1 leads to: $D_{U,\,corr} = D_U / (f\ [Qtz] + [kao])$

Taking for instance $C_{qtz} = 0.9$, $C_{kao} = 0.1$, $r = 50\ \mu m$, $d = 20\ \mu m$ one obtains:

$a = 0.4$, $f = 0.784$ and $D_{U,\,corr} = 1.24 \times D_U$

Table SI 6: Estimated radius of quartz grains with assumed spherical shape

Sample	Material	Thin section	Estimated Quartz Radius (μm)
P1-150* FT	Soil	X	10
P1-300	soil		10
P1-350* FT	sdt	X	37
P1-530	sdt		50
P1-620*	sdt		37
P1-760* FT	sdt	X	20
P2-20	soil		10
P2-150	soil		10
P2-240*	soil		10
P2-530* FT	sdt	X	100
P2-660	sdt		50
P2-900	sdt		50
P3-210	sdt		25
P3-465 FT	sdt	X	25
P4-50*FT	soil	X	10
P4-1000* FT	sdt	X	50

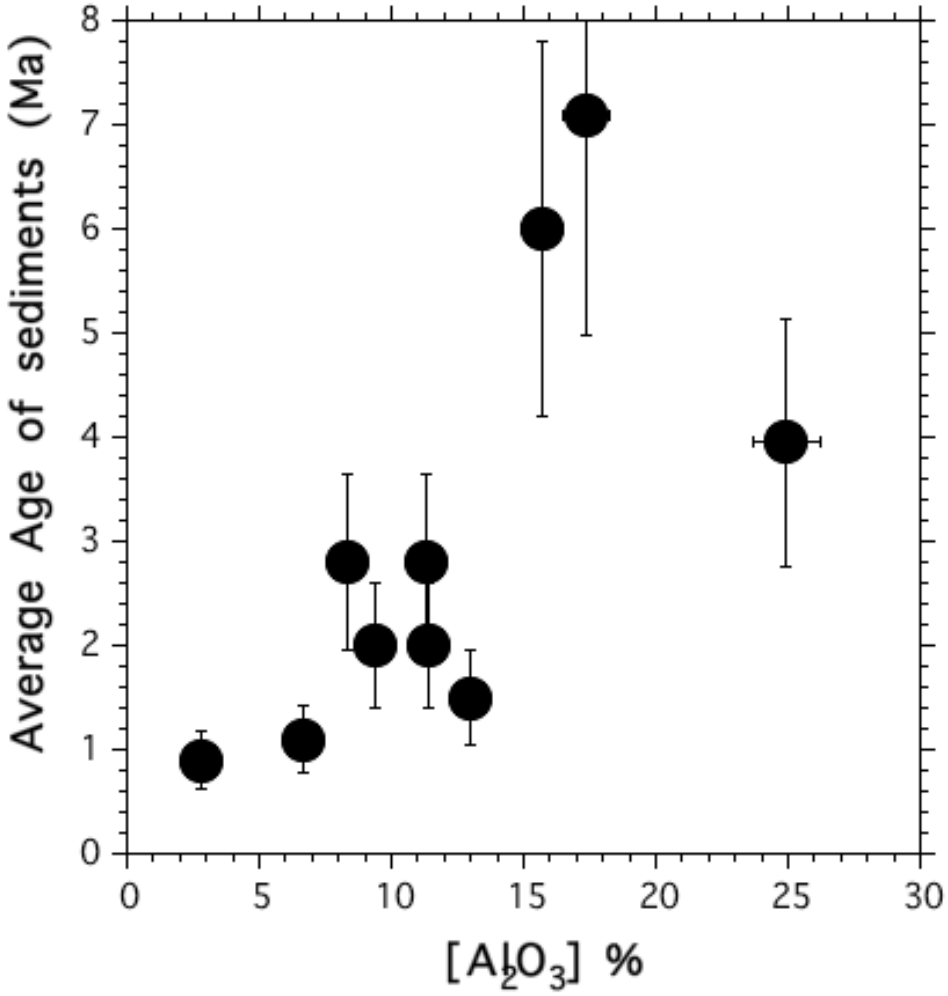

Figure SI 7: Relation between the age of kaolinites in sediments and the clay content assessed by the Al_2O_3 concentration. The increasing trend suggests processes of (re)crystallization of kaolinites favored by low clay contents (i.e. expected higher porosity).